











Lithium-doped two-dimensional perovskite scintillator for wide-range radiation detection

Aozhen Xie ^{1,2}, Chathuranga Hettiarachchi², Francesco Maddalena¹, Marcin E. Witkowski ³, Michał Makowski ³, Winicjusz Drozdowski ³, Arramel Arramel ⁴, Andrew T. S. Wee ⁴, Stuart Victor Springham ⁵, Phan Quoc Vuong ⁶, Hong Joo Kim⁶, Christophe Dujardin ⁷, Philippe Coquet^{1,2,8}, Muhammad Danang Birowosuto^{1,2}✉ & Cuong Dang ^{1,2}✉

Two-dimensional lead halide perovskites have demonstrated their potential as high-performance scintillators for X- and gamma-ray detection, while also being low-cost. Here we adopt lithium chemical doping in two-dimensional phenethylammonium lead bromide (PEA)₂PbBr₄ perovskite crystals to improve the properties and add functionalities with other radiation detections. Li doping is confirmed by X-ray photoemission spectroscopy and the scintillation mechanisms are explored via temperature dependent X-ray and thermoluminescence measurements. Our 1:1 Li-doped (PEA)₂PbBr₄ demonstrates a fast decay time of 11 ns (80%), a clear photopeak with an energy resolution of 12.4%, and a scintillation yield of 11,000 photons per MeV under 662 keV gamma-ray radiation. Additionally, our Li-doped crystal shows a clear alpha particle/gamma-ray discrimination and promising thermal neutron detection through ⁶Li enrichment. X-ray imaging pictures with (PEA)₂PbBr₄ are also presented. All results demonstrate the potential of Li-doped (PEA)₂PbBr₄ as a versatile scintillator covering a wide radiation energy range for various applications.

¹CINTRA UMI CNRS/NTU/THALES 3288, Research Techno Plaza, 50 Nanyang Drive, Border X Block, Level 6, Singapore 637553, Singapore. ²School of Electrical and Electronics Engineering, Nanyang Technological University, 50 Nanyang Avenue, Singapore 639798, Singapore. ³Institute of Physics, Faculty of Physics, Astronomy, and Informatics, Nicolaus Copernicus University in Torun, ul. Grudziadzka 5, Torun 87-100, Poland. ⁴Department of Physics, National University of Singapore, 2 Science Drive 3, 117542 Singapore, Singapore. ⁵Natural Sciences and Science Education, National Institute of Education, 637616 Singapore, Singapore. ⁶Department of Physics, Kyungpook National University, Daegu 41566, Korea. ⁷Université de Lyon, Université Claude Bernard, Lyon 1, CNRS, Institut Lumière Matière UMR5306, Villeurbanne F-69622, France. ⁸Institut d'Electronique, de Microélectronique et de Nanotechnologie (IEMN), CNRS UMR 8520-Université de Lille, Villeneuve d'Ascq 59650, France. ✉email: mbirowosuto@ntu.edu.sg; hcdang@ntu.edu.sg

The research on lead halide perovskite (referred to here as 'perovskite') for X-ray or gamma-ray detection has been rapidly expanding. On one hand, employing methylammonium lead iodide (MAPbI₃) as the active material in a solar cell configuration shows good performance in X-ray photon to electron conversion^{1–4}. On the other hand, the idea of a perovskite scintillator emerged as early as 2008 but did not receive much attention until the wide application of perovskite in high-energy radiation detection⁵. The former detection is direct and straightforward with simple conversion photons to electrons. However, to efficiently extract the free carriers, other transport layers are required, and the perovskite absorber layer requires to be thin which makes the device complicated to fabricate and less efficient to absorb X-ray photons. Compared with the former, scintillation detection requires only the scintillator crystal and integrated visible light detection hardware like charge-coupled devices or complementary metal-oxide-semiconductors, which are commercially available and low cost. There is a great demand in the scintillator market for medical imaging, scientific research and security, and new challenges makes the research still very active^{6,7}. Current commercial scintillators are bulk crystals and their synthesis usually require temperature ranging from 621 °C for CsI:Tl up to more than 2000 °C for Lu₂SiO₅:Ce³⁺ (LSO) using Bridgman or Czochralski growth⁸. The huge energy consumption to generate and maintain such high temperatures hinders the reduction of production costs.

The intrinsic heavy atom Pb in perovskite and the possibility of low-temperature and solution-processing fabrication allow perovskite to be a candidate for next generation scintillator. Besides, it is reported that the organic-inorganic hybrid perovskite demonstrates a good radiation stability under gamma-ray at least compared with inorganic glass⁹. In terms of crystal structure, perovskites can be classified as three-dimensional (3D) and two-dimensional (2D). It is generally believed that 2D ones have higher light yield and faster decay due to their higher exciton binding energy (hundreds of meV) compared with 3D ones (tens of meV)^{10,11}. High-energy alpha particle detection and the potential X-ray imaging applications with 2D perovskite single-crystal scintillators have never been reported. We note that recently 3D perovskite CsPbBr₃ nanocrystals¹² and nanosheet¹³ have demonstrated good performance as scintillator screen in X-ray imaging. However, the inherent chemical instability and low density of composite made of nanomaterials (inadequate radiation stopping) is an obstacle in practical applications where low doses are required. 2D bulk crystals in this scenario could be another option because they possess the benefits mentioned above and they are free from such disadvantages. Doping could be a useful approach to modify or boost some scintillator performance¹⁴. Li dopant has been reported for modification of optical properties¹⁵ and reduction of nonradiative loss in perovskite exciton recombination¹⁶. Electrochemical doping of Li was achieved to lower the threshold voltage for perovskite LED¹⁷. The introduction of ⁶Li can bring a completely new functionality, thermal neutron detection because of the intrinsic high thermal neutron capture of ⁶Li isotope¹⁸. Thermal neutron detection plays an important role in neutron scattering research¹⁸, landmine detection¹⁹, and oil logging²⁰. However, current thermal neutron scintillators also suffer from the high cost of the high-temperature processing. A recent report of the 2D semiconductor ⁶LiInP₂Se₆ for first-time direct thermal neutron detection provided a new direction, but this direct detection mode is still far from commercialization and wide application for neutron imaging²¹. It will be of interest to combine the merits of 2D perovskite and Li dopant to develop low-cost X-/gamma-ray scintillators with extra thermal neutron detection capability, and investigate the properties changes or develop new scintillator behaviors.

In this work, we synthesized Li-(PEA)₂PbBr₄ perovskite crystals which are characterized under different types of radiation. We also tested its capability to discriminate between gamma-ray and alpha particle. Finally, we demonstrate the employment of our perovskite in X-ray imaging. After temperature-dependent X-ray luminescence and X-ray thermoluminescence characterizations, it is concluded that Li ions being trapped in the crystal pose their impact on enhancing while broadening the emission. Under 662 keV gamma-ray, the light yield of Li-(PEA)₂PbBr₄ is up to 11,000 photons per MeV (ph per MeV) with a fast-primary decay time of 11 ns. Successful detection of alpha particle, in conjunction with reasonable discrimination between gamma ray and alpha particle, demonstrates the potential of Li-(PEA)₂PbBr₄ crystal in neutron detection. With 8 keV soft X-ray, X-ray phase-contrast images were obtained using our perovskite as the scintillator screen. Our study suggests the potential of Li-(PEA)₂PbBr₄ as a versatile scintillator in wide-range energy radiation detection.

Results and discussion

Crystal structure and Li-doping characterizations. Compared with 3D perovskite, the layered structure of (PEA)₂PbBr₄ introduces the quantum confinement effect¹¹. In this case, large binding energy (hundreds of meV versus tens of meV in the 3D counterpart) favors excitonic recombination and thus theoretically enhances luminescence²². The key to transforming a 3D lead halide perovskite into a 2D one is the introduction of a long alkyl chain or bulky organic cation, such as n-butylammonium, 2,2'-(ethylenedioxy)bis(ethylammonium)²³, and 3,4,5-Trifluoroaniline ammonium²⁴. In our experiment, the phenethylammonium cation is chosen due to its high chemical stability, commercial availability, and fast scintillation^{5,25}. The structure of (PEA)₂PbBr₄ is shown in Fig. 1a. The alternating inorganic/organic layers effectively confine the exciton inside the inorganic layer and thus benefit the scintillation under high-energy radiation like gamma-ray²⁵. Figure 1b shows the optical images of the 1:1 Li-(PEA)₂PbBr₄ crystals. The size of the tilted hexagonal-shape crystal can be up to 1 × 0.7 × 0.2 cm³ due to the slow evaporation method. Although some grains and boundaries exist, the transparency is still satisfactory as all the assigned letters below the crystal can be seen clearly. Under UV (365 nm) and X-ray (Cu Kα, 8 keV) excitation, the crystal shows a bright purple-blue emission which indicates high crystal quality. Our blue emission brightness is comparable to that of recent 1D Rb₂CuBr₃ under 30 keV X-ray radiation²⁶. The powder X-ray diffraction (XRD) result is demonstrated in Fig. 1c. The experimental XRD pattern is comparable to the powder diffraction pattern simulation from the corresponding crystallographic information file (Supplementary Fig. 1)²⁷. No substantial peak shift can be found except a slight intensity ratio of the (020) peak at 15.4° and the (003) peak at 15.9° decreases from undoped to highest 1:1 Li-(PEA)₂PbBr₄ crystals. The absence of large difference in XRD implies Li dopant induced little lattice distortion. There are two reasons behind this observation. On one hand, Li is a light element and its X-ray cross section is smaller than the other elements. On the other hand, Li atom is so small that it is unlikely to cause large lattice distortion while the Li concentration is relatively low in the crystal, which is confirmed by the X-ray photoelectron spectroscopy (XPS) and inductively coupled plasma mass spectrometry (ICPMS) results demonstrated in Fig. 1d (see also Supplementary Fig. 2 and Supplementary Table 1). In our experiment, we used (PEA)₂PbBr₄ crystals with different Li-doping concentrations at comparable size and thickness, allowing us to make direct qualitative and quantitative comparisons. As the Li/Pb precursor ratio increases, the Li/Pb XPS integrated

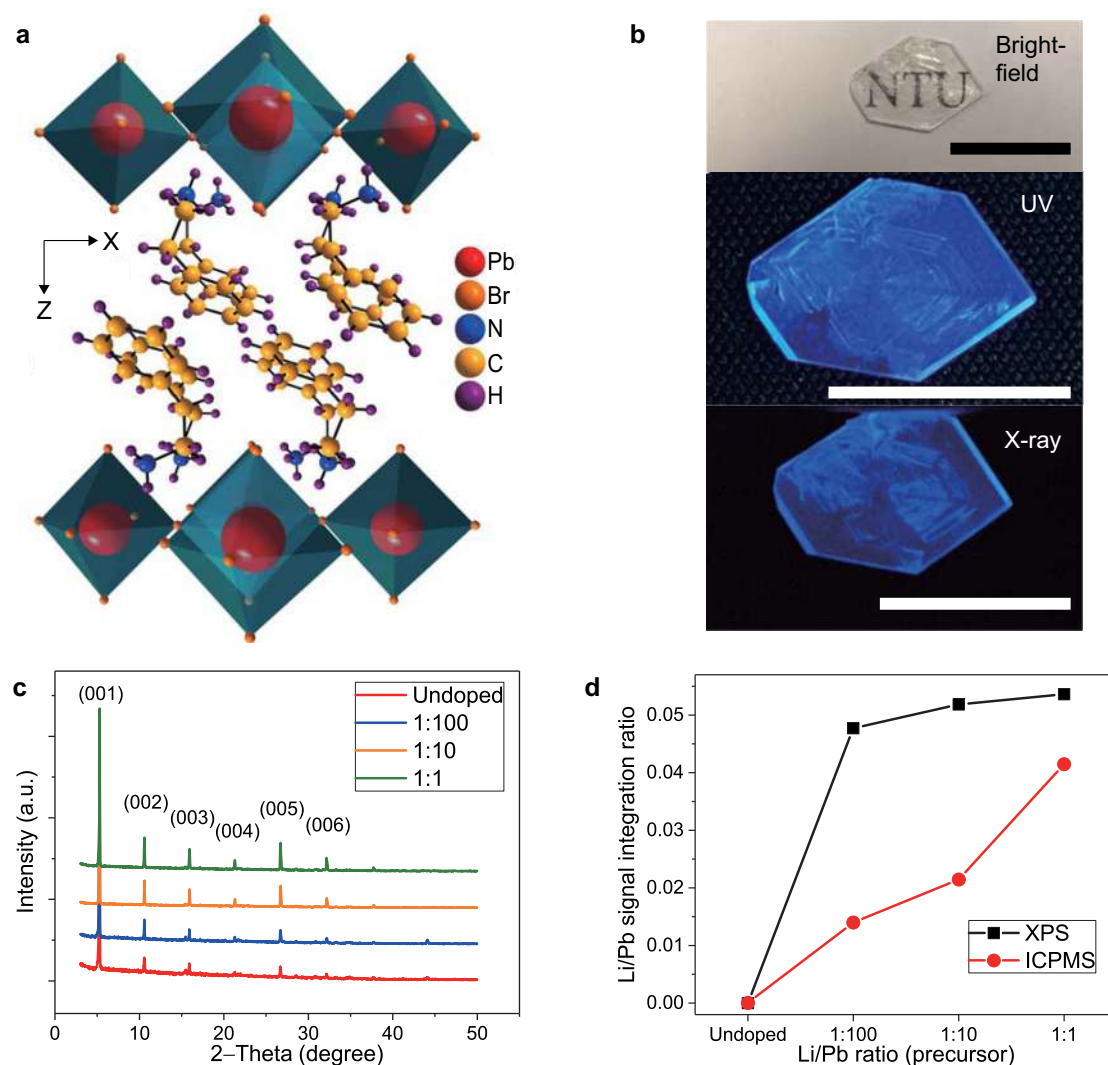


Fig. 1 Crystals structure, luminescence, and Li-dopant concentration characterization. **a** Crystal structure of $(\text{PEA})_2\text{PbBr}_4$ ^{58,59}. **b** Bright-field, UV and X-ray images of 1:1 Li- $(\text{PEA})_2\text{PbBr}_4$ single crystal. The lengths of black and white bars are 1 cm. **c** Powder XRD pattern of four different Li-doped crystals. **d** Li to Pb XPS and ICPMS signal ratios as a function of precursor ratio.

intensity ratio from the crystals rises from undoped to 1:100 and then gradually reaches a plateau. According to integration of different elements, we estimate that the Li/Pb ratio is 5% in the highest doping 1:1 Li-doped crystal. ICPMS suggests also a similar 4% Li/Pb ratio in the highest doped 1:1 crystal but they are variations in 1:100 and 1:10 crystals compared with XPS result. The differences can be attributed to different element detection sensitivity because of varied detection mechanisms, but we consider that they are still reasonable, because the absolute differences are not large as well as the low concentration and intrinsic light atom properties of Li may cause insensitivity in these characterizations. The natural abundance of ^6Li , of interest for thermal neutron capture is 7.59%, and thus the ^6Li percentage is around 0.38% in 1:1 Li-doped crystal using the 5% Li/Pb XPS ratio. In our experiment, while we increased the Li/Pb ratio exponentially in the precursor solutions, the Li/Pb ratio in the corresponding crystals increased only marginally. We suggest that it is difficult to control the actual Li-doping level as we expected by simply adding more dopant precursor.

Temperature-dependent X-ray luminescence. Based on the above XPS and ICPMS results, the existence of Li dopant within the perovskite is verified. Therefore, we proceed to investigate the

influence of Li in temperature-dependent X-ray luminescence (XL) spectra. Here the undoped and the 1:1 Li-doped crystals are chosen and compared because their representative emission contrast is quite distinctive under X-ray excitation. Figure 2a, b shows the XL comparison between two representative high and low temperatures (330 and 10 K) from undoped and 1:1 Li-doped crystals (1:100 and 1:10 in Supplementary Fig. 3). Both free exciton (FE) emissions at 418 nm are shifted to 436 nm from 10 to 330 K²⁸. XL spectra at 10 K from both crystals show a bump ranging from 450 to 750 nm. We consider this bump corresponds to the self-trapped exciton (STE) emissions although STE in (001) type 2D perovskite are scattered. There are two reasons we attribute the broad peaks at low temperature to STE. First, STE in (001) type can be temperature-dependent in which STE only emerges at low temperature²⁹, and that is what we observed in the spectra. Second, dopant in 2D perovskite could possibly trigger the occurrence of STE³⁰. However, the intensity ratio between FE emission and the STE emission (denoted as FE/STE ratio) is much higher in a 1:1 crystal than in undoped one. Theoretically, higher Li concentration should create more traps and thus more likely to have stronger STE emission. In fact, Li being traps is indeed confirmed by the following X-ray excited thermoluminescence (TL) measurements. In this case, Li dopant could

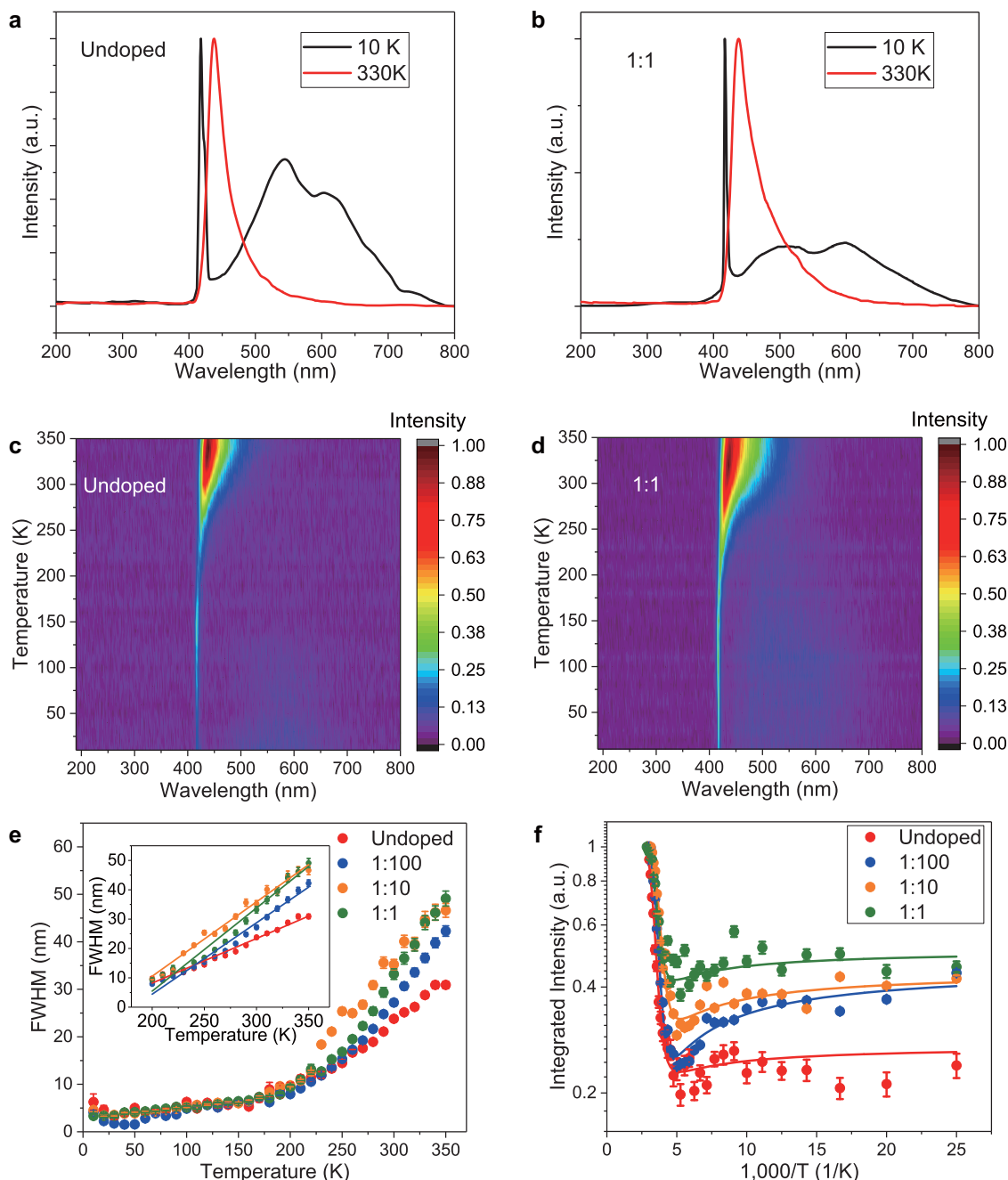


Fig. 2 Temperature-dependent X-ray luminescence. X-ray luminescence spectra at representative temperature, 10 and 330 K from **a** undoped and **b** 1:1 Li-(PEA)₂PbBr₄. Temperature-dependent X-ray luminescence spectra from 10 and 350 K from **c** undoped and **d** 1:1 Li-(PEA)₂PbBr₄. **e** Comparison of FWHM versus temperature among different Li-doped crystals. **f** Comparison of the negative thermal quenching behavior.

bring three possible effect on FE and STE quenching or enhancement at 10 K. The first possibility is Li dopants enhance both FE and STE but impose stronger effect on FE. The second possibility is Li dopants quench both FE and STE but have stronger effect on STE. The final possibility is Li dopant enhances FE while quench STE. Supplementary Fig. 4 demonstrates that all doped crystals have higher intensity than undoped ones at 10 K, so it is unlikely for Li dopant to quench both FE and STE. Then we can compare the normalized 2D map temperature-dependent XL of undoped and 1:1 Li-doped crystals in Fig. 2c, d (1:100 and 1:10 in Supplementary Fig. 5). We can see the bump in from 1:1 crystal survives up to 200 K and thus Li dopant does not quench STE. Our first proposition of Li dopant may enhance both FE and

STE seems more suitable to our observations. The emission peaks at 330 K are asymmetric, which we believe it is due to part of the emission being re-absorbed and confirmed by the UV absorption and emission spectrum (see Supplementary Fig. 6) since the X-ray luminescence shares a similar exciton emission mechanism to the UV photoluminescence. The emission peak is shifted from 405 nm in PL to 436 nm in XL. This redshift behavior also occurs for three-dimensional CsPbBr₃ perovskite single crystal. In addition, we can find the full width half maximum (FWHM) of undoped is smaller than that of 1:1. By comparison of this series of crystals, FWHM at 330 K increases gradually from undoped to 1:1 (undoped: 30 nm, 1:100 doped: 41 nm, 1:10 doped: 46 nm, and 1:1 doped: 50 nm). The effect of Li is apparent in broadening the

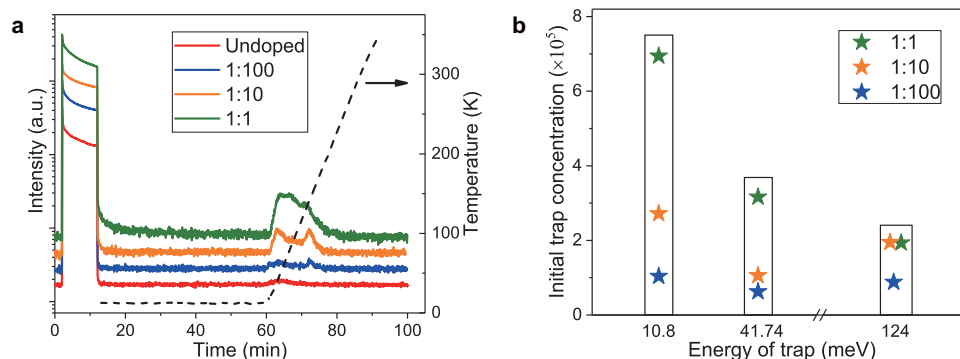


Fig. 3 Thermoluminescence and energy traps. **a** X-ray thermoluminescence plots of undoped, 1:100, 1:10, and 1:1 Li-(PEA)₂PbBr₄. The dashed line indicates the rise of temperature. **b** Initial trap concentration at corresponding energy from 1:100, 1:10, and 1:1 Li-(PEA)₂PbBr₄. For clarity, the symbols of 1:10 and 1:1 are intentionally separated due to their close values.

emission, besides enhancing the emission intensity. In Fig. 2c, d, from 200 to 10 K both emission peaks are narrow and almost symmetric and STE emissions exist. But the difference in peak position or FWHM is quite small between undoped and doped due to strong narrowing effect by lowering temperature³¹. Figure 2e plots the quantitative comparison of FWHM evolution upon cooling. No substantial variation can be seen below 200 K and above 200 K, the slope starts differing as a result of Li dopant. A simple linear fitting can be employed to quantify the difference. The slope values increase considerably from undoped to 1:1 but level off (undoped: 0.15, 1:100 doped: 0.24, 1:10 doped: 0.25, and 1:1 doped: 0.28, unit, nm per K) and such behavior agrees well with the integrated ratio profile in XPS analysis in Fig. 1d.

The more interesting part of the 2D maps is the stronger emission upon higher temperature, as shown in Fig. 2f. Such behavior has been reported earlier in photoluminescence (PL) of n-type GaAs and n-type ZnS and it was termed as the negative thermal quenching effect³². This effect is commonly originated from thermally excited traps³². A similar phenomenon in temperature-dependent PL of (PEA)₂PbBr₄ microplate was observed³³. Negative thermal quenching is almost the opposite to the thermal quenching in our previous report on methylammonium lead halide perovskite single crystals using the same setup, where the emissions become stronger monotonically as temperature goes down to 10 K³¹. In this scenario, the strongest emission occurs at 350 K, the highest temperature in this experiment. As cooling continues, the emissions reach their minima at around 220–200 K. Below 200 K, slowly the emissions become slightly stronger compared with their minima and the STE emissions begin to appear. This effect is enhanced with Li doping. The curves of Li-doped crystals are “lifted up” compared with the undoped one. The integrated intensity ratios between the minima and the maxima (~350 K) can be a parameter to define the enhancement induced by Li. Other parameters of the negative thermal quenching fits are presented on Supplementary Table 2 (see Supplementary Discussion 1 for details). With increasing Li concentration, this ratio increases from lowest undoped to highest 1:1 doped (undoped: 0.23, 1:100 doped: 0.25, 1:10 doped: 0.32, and 1:1 doped: 0.42). Although the magnitude of the enhancement is small, it indicates the relative wide-range emission stability of our Li-(PEA)₂PbBr₄. The strongest emission is rarely above 300 K in lead halide perovskite because thermal quenching dominates and prevents excitonic recombination at that temperature. It is reported that most of the strongest emission from materials with negative thermal quenching behavior occurs at around 100–200 K for typical II–VI or III–V semiconductor composites³²; while it is considerably lower than 300 K for other 3D perovskites or perovskite nanocrystals/quantum dots without

extra protection^{33–35}. Such stronger emission upon higher temperature characteristics allows (PEA)₂PbBr₄-based detectors to operate at up to 350 K or even higher. The continuous luminescence change suggests the absence of temperature-induced phase transition³⁶. Instead of making it worse upon rising temperature, the addition of Li dopant increases the stability of the intensity or the radiation-converted photons with the temperature. Beside the later function of Li dopant with other radiation detection, the addition of concentration already makes Li-(PEA)₂PbBr₄ even more competitive compared with the other perovskites mentioned above (3D or nanocrystals) since the Li-(PEA)₂PbBr₄ scintillator performs well at a wide range of temperatures, and no extra cooling is required to maximize its emission and light yield.

X-ray excited thermoluminescence and afterglow. After a detailed discussion on the emission properties of Li-(PEA)₂PbBr₄, we continue presenting an insight on the role of Li as trap agent using X-ray excited TL characterization. Figure 3a demonstrates the comparison of normalized TL curves. After 10 min X-ray exposure at 10 K, the emission was monitored for 100 min. We find two changes induced by Li doping. The most prominent change is that the thermoluminescence peaks (after 3600 s) become more intense upon higher Li doping. To analyze these TL peaks, the classic Randall–Wilkins equation³⁷ can be employed to deconvolute the peaks:

$$I = \sum_{i=1}^3 n_{0i} s_i \exp\left(-\frac{E_i}{k_B T}\right) \exp\left(-\frac{s_i}{\beta} \int_{T_0}^T \exp\left(-\frac{E_i}{k_B T'}\right) dT'\right) \quad (1)$$

where I is the TL intensity, 3 is the number of deconvoluted peaks, n_{0i} is the initial trap concentration, s_i is the frequency factor, E_i is the trap depth, k_B is the Boltzmann constant, β is the heating rate, T is the temperature, and T_0 is the initial temperature. The TL peaks of the undoped samples do not exhibit any appreciable fitting. For the other crystals, the TL peaks can be deconvoluted into three peaks and the parameters are listed in Supplementary Table 3. Figure 3b displays the concentration of three types of trap with different energy depths. It is clear that there are more traps at different energy depths with higher Li doping from 1:100 to 1:1. The total number of traps is comparable to the reported value from photocurrent measurements ($10^5 \sim 10^7 \text{ cm}^{-3}$)³. Shallow traps (10.8 meV) are the major contribution to the total increase of traps induced by Li doping, while deep traps (124 meV) show a smaller contribution. The other difference is that small after-glow effects can be barely seen in undoped and 1:100 doped crystals, while they become more

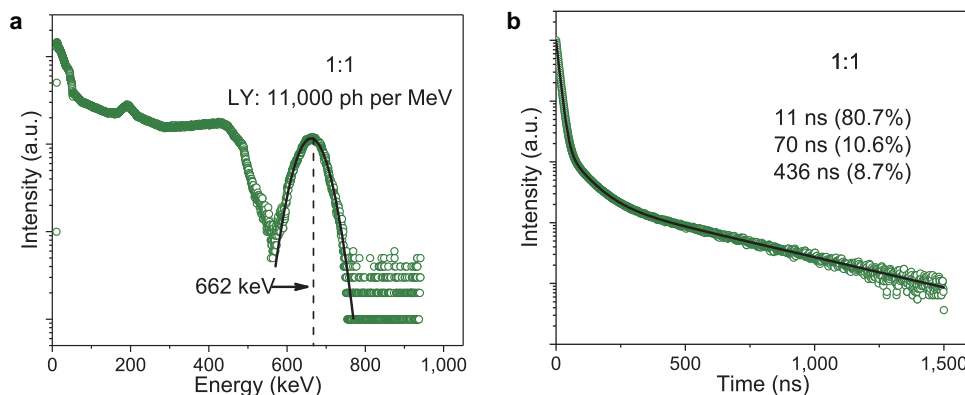


Fig. 4 Gamma-ray excitation characterizations. **a** Gamma-ray pulse-height spectra and **b** gamma-ray excited decay of 1:1 Li-(PEA)₂PbBr₄. Black line in **(a)** is the Gaussian fitting for extraction of light yield and energy resolution and in **(b)** is the three-component exponential decay fitting.

pronounced in 1:10 and 1:1 (Supplementary Fig. 7). We attribute this behavior to additional traps generated by Li doping. After these characterizations, we establish that Li serves as traps in the (PEA)₂PbBr₄ scintillation under X-ray irradiation and it may enhance performance while broadening the luminescence.

Gamma-ray pulse height and scintillation decay time. Beside soft X-ray characterization, we further explore scintillation properties under gamma-ray radiation. As temperature-dependent XL shows that the radiation-converted photons are optimized at room temperature, we still need to determine the scintillation light yield. This number is obtained through the comparison of the photopeak signals in the pulse-height spectra at certain energy of gamma-ray radiation with the scintillator single electron response, see the “Methods” section. Figure 4a exhibits the pulse-height spectra of 1:1 crystal with ¹³⁷Cs (662 keV). The light yield and the energy resolution are 11,000 ± 500 ph per MeV and 12.4%, respectively. For the other doped crystals, the light yield of 1:100 and 1:10 are 6300 ± 300 and 9100 ± 400 ph per MeV, while their energy resolutions are 32.6% and 36.8%, respectively (Supplementary Fig. 8). The light yield of undoped crystal is 8000 ± 800 ph per MeV. Our light yield values here are determined by traditional gamma-ray pulse-height measurements compared with those estimated by the integral of the X-ray luminescence intensities demonstrated previously for perovskite scintillators^{12,26}. We can see a general tendency of increasing light yield with higher Li concentration although the light yield of undoped is marginally higher than 1:100. We consider that it is due to slightly different crystal quality. Crystal quality, including crystal morphology, transparency and homogeneity plays a critical role on quality-sensitive pulse-height measurement. Unfortunately, crystal quality control is not easy since there is no mature 2D perovskite crystal growth technique from solution method compared with 3D ones^{38,39}. However, it is reasonable that there is no dramatic increase in light yield with more Li since the XPS result manifest close Li concentration in all doped crystals. The energy resolution is also affected by crystal quality. According to our calculation based on Poisson statistics of the photoelectron, the energy resolution of 1:1 crystal can be as low as 6% theoretically^{40–42} (see Supplementary Discussion 2) and hence there is considerable room for energy resolution improvement. The gamma-ray excited decay measurement result of 1:1 is shown in Fig. 4b. A three-component exponential decay was adopted in the fitting. The percentages of decay in this experiment are all in amplitude. The primary (fast) decay time (11 ns) is similar to early reports (9–11 ns)^{25,38}. At this stage, it is difficult to confirm the doping effect on decay time and we tentatively see no significant effect is induced by the Li content since

their values are comparable to one another and to other reports (see Supplementary Fig. 9). Compared with the popular commercial NaI:Tl scintillator, the highest light yield of our Li-(PEA)₂PbBr₄ is lower (11,000 vs. 38,000 ph per MeV), while the primary decay time is one order of magnitude smaller (11 vs. 250 ns) at room temperature⁸. It indicates that the time density of photons at early stage of the pulse is significantly higher, making Li-(PEA)₂PbBr₄ advantageous for fast timing applications such as high-speed imaging and image processing applications.

Alpha particle, gamma-ray, and thermal neutron radiation discrimination. In addition to X- and gamma-ray, we took a step further to test our Li-(PEA)₂PbBr₄ crystals for alpha particle (⁴α) detection. Figure 5a displays the result of alpha particle pulse-height characterization of 1:1 Li-doped crystal using ²⁴¹Am (5486 keV) and ²⁴⁴Cm (5805 keV) as the alpha particle sources. Results of other radioisotope sources are also presented in Supplementary Fig. 10. We can easily distinguish the two full-energy peaks although they are relatively broad. To the best of our knowledge, this is the first time the successful application of 2D perovskite scintillator in alpha particle detection has been reported^{43–45}. The full-energy peaks indicate the potential thermal neutron detection on the alpha particle as a product from the ⁶Li (n, α) reaction⁴⁶. Also, there is an opportunity for fast neutron detection by virtue of the considerable amount of hydrogen and Li dopant in the future Li-doped perovskite crystal⁴⁶. However, the discrimination with other radiations will be more complicated if we add more hydrogen amounts in the crystals. It can be a choice of material for neutron diagnostics in inertial confinement fusion requiring fast neutron detection and back scattering on Li ions⁴⁷. Figure 5b shows the sign for pulse-shape discrimination (PSD) with our Li-(PEA)₂PbBr₄ crystal using the optimum filter method⁴⁸ based on the significant difference between the scintillation decay under alpha particle and gamma-ray excitation (Fig. 5b inset). Alpha particle signals in high-energy channels is quite well separated from gamma-ray ones. However, the alpha particle full-energy peak was broad and the tail at low energy channel is slightly overlapped with the gamma-ray signals. It can be a result of insufficiently high crystal quality and aggravated by the defect layer on the surface of the crystal as the crystal could be degraded through long-time MeV alpha particle bombardment in this measurement. In our previous report of 3D halide perovskite scintillators, dose-dependent XL measurements reveal that radiation dose up to 1 millisievert for one hour has a weak impact on the light yields of bromide perovskite scintillators³¹. We could reasonably expect a similar X-ray radiation hardness of our (PEA)₂PbBr₄ crystals and good stability over time at low dose.

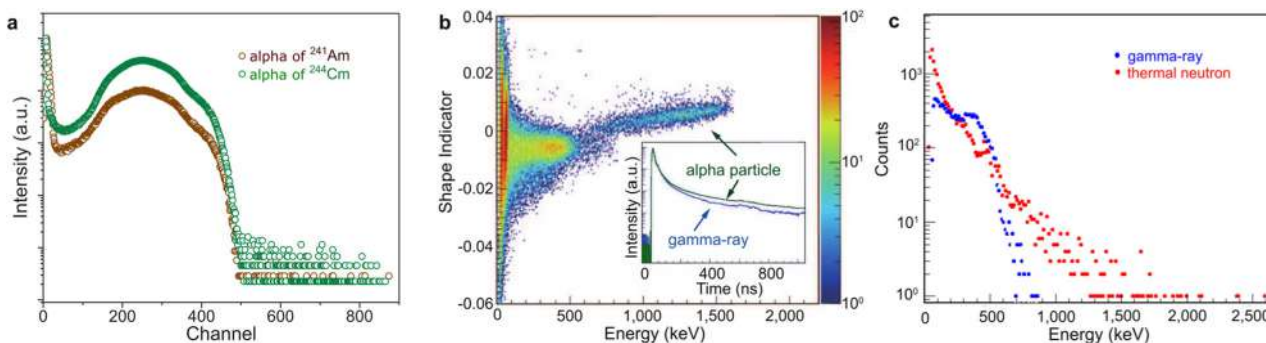


Fig. 5 Alpha particle detection and discrimination between thermal neutron and gamma ray. **a** Alpha particle pulse-height spectra. **b** Pulse-shape discrimination (PSD) matrix with the shape indicator on *y*-axis and the measured energy (electron equivalent) on *x*-axis. The inset with the green and the blue curves shows the normalized average waveforms from both alpha particle and gamma-ray radiation of ^{137}Cs and ^{241}Am sources, respectively. **c** Pulse-height spectra measured with graphite-moderated Am–Be neutron source of 1:1 Li-(PEA) $_2$ PbBr $_4$ crystal. The pulse-height spectra of neutron and ^{137}Cs sources are indicated by red and blue dots, respectively.

However, decreases in light yields and energy resolutions in pulse-height spectra were indeed observed after long-time exposure of much higher energetic radiation (see Supplementary Fig. 11). Despite the small signal overlap, the demonstration of PSD discrimination between alpha particle and gamma-ray verifies the potential of thermal neutron detection with our Li-doped 2D perovskite. It is known that thermal neutron detection usually requires the detection of neutron-induced secondary radiation, especially for readily detected charged particles like alpha particle⁴⁶. However, the process of neutron generation is usually accompanied by gamma-ray background. That is the reason why it is critical to exploit the capability of discriminating between alpha particle and gamma-ray using the PSD method^{49,50}, which is not demonstrated by the recent neutron semiconductor detection²¹. The quenching factor (α/β ratio), which is determined by the number of photons per MeV produced by one alpha particle over the number of photons per MeV produced by one electron (photoelectric effect by gamma ray in this case), was estimated to be 0.24⁵¹. Using this result, we can also discriminate between thermal neutrons and gamma-ray and it is expected that the thermal neutron signal will appear at energy larger than 1.5 MeV. However, as ^6Li is only 7.59% in natural abundance²¹ while the Li content in this crystal is only 5%, it is expected that we cannot observe the strong thermal neutron full-energy peak but only a bump in our experiment as demonstrated in Fig. 5c. In addition, at this current stage, the crystal quality also needs to be improved so that it can compete with the energy resolution of Cs $_2$ LiYCl $_6$:Ce $^{3+}$ crystals⁵². Besides, the theoretical thermal neutron detection efficiency maximum of natural and ^6Li -enriched 1:1 Li-(PEA) $_2$ PbBr $_4$ are 7% and 48%, respectively (see Supplementary Discussion 3 and Supplementary Table 4). The 48% efficiency is still comparable to natural Li-containing elpasolite single-crystal scintillators in an early report⁵³. Therefore, further growth of cm-scale thicker crystals with higher ^6Li content are necessary to improve the thermal neutron detection (see Supplementary Fig. 12).

X-ray imaging with Li-(PEA) $_2$ PbBr $_4$ scintillator. Finally, to demonstrate the X-ray scintillation imaging application, X-ray phase-contrast imaging of a ubiquitous safety pin was carried out using Li-(PEA) $_2$ PbBr $_4$ as a scintillator film. The schematic setup is displayed in Fig. 6a. The safety pin was put inside an envelope as the test subject. The 1:1 Li-(PEA) $_2$ PbBr $_4$ spin-coated film with a thickness of 67 μm (Supplementary Fig. 13) that was prepared by our new technique shows high transparency and satisfying homogeneity, despite some small surface ripples (Fig. 6b). Typical

spin-coating and baking techniques were found to be ineffective in acquisition of a homogeneous thick film (up to 50 μm or above for effective X-ray stopping), which is required in the X-ray characterization (see Supplementary Discussion 4)⁵⁴. To get a thick film, spincoating at low speed (<500 rpm) usually results in an inhomogeneous film. Inspired by a reported spin-coating technique by introducing N $_2$ flow during spincoating, we modified it and blow-dried the film with hot air flow in the last stage of spin-coating⁵⁵. This technique proved to be very useful and a relatively thick and homogeneous film on glass substrate was obtained. One great merit in (PEA) $_2$ PbBr $_4$ should be highlighted here; that is, its intrinsic readiness to form on average mm-size large single-crystal flakes upon drying. It follows that the film is composed of large orientated single-crystal 2D flakes instead of the small un-orientated small crystals which are common in 3D perovskite spin-coated film. The powder XRD verifies the same crystal phase of the spin-coated film as the single crystal (see Supplementary Fig. 1). Longer exposure time (3 s) for the spin-coated film was needed to achieve comparable brightness to the thick crystal in Fig. 1b (~400- μm thickness, 1 s) under X-ray radiation. Despite such circumstances, decent X-ray pictures can be secured as the thickness of 67 μm is enough to stop X-ray radiation, see Supplementary Fig. 14. Due to the substantial difference in X-ray stopping power (Cu K α , 8 keV) between the envelope and the stainless steel, the fine structure of the safety pin, like a 250- μm slit, is revealed clearly by an ordinary camera as shown in Fig. 6c. Here, the black and white mode was utilized for better contrast. Other items like a spring or a paper clip can be clearly imaged under X-ray as well (Supplementary Fig. 15). Though there are quite a few researches on the scintillation properties of (PEA) $_2$ PbBr $_4$ under X-ray or gamma ray^{25,38}, here we demonstrate the first imaging using this perovskite material as far as we know. The quality of the imaging compared with those of CsPbBr $_3$ ^{12,13} is still lower as our camera is not optimized for the blue emission of the scintillators. Moreover, the configuration of the imaging is different as we did not couple the scintillator directly on the photodetector. However, the convenient coupling of our cost-efficient film with the commercial camera is already applicable in high-throughput security inspection. The film can be even further optimized for a smoother surface and higher thickness in the future and a performance improvement can be expected, such as higher and more homogeneous scintillating brightness and shorter exposure time for reduced noise.

In summary, we demonstrated successful Li doping in (PEA) $_2$ PbBr $_4$ crystal synthesis using a solution-processing method. Li-dopant serving as traps is capable of enhancing the intensity while broadening the X-ray luminescence. The intrinsic

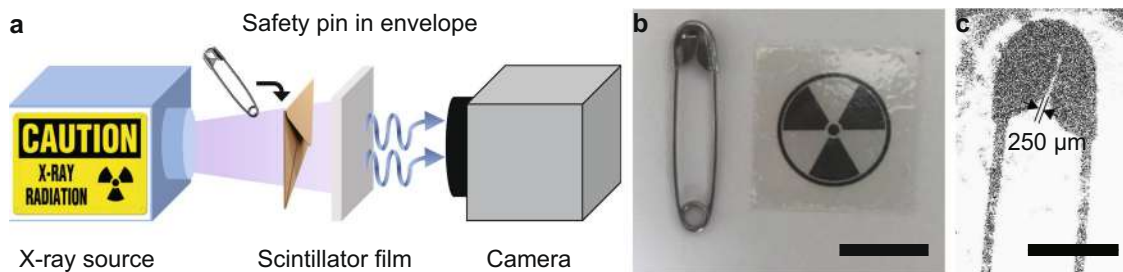


Fig. 6 X-ray imaging performance. **a** Scheme of X-ray imaging setup using 1:1 Li-(PEA)₂PbBr₄ as scintillator. The safety pin is inside the envelope. **b** Bright-field image of the safety pin and the Li-(PEA)₂PbBr₄ film on glass substrate with high transparency. Scale bar is 1 cm. **c** X-ray image (background corrected) of the safety pin. Black and white mode was applied for better contrast. Scale bar is 5 mm.

negative thermal quenching behavior of (PEA)₂PbBr₄ allows it to maintain its scintillating performance at a relatively wide range of temperature; however, with additional Li dopant, the performance stability could be even more improved. We found that Li ion dopant could increase the light yield up to 11,000 ph per MeV while maintain a primary decay time (11 ns) under 662 keV gamma-ray radiation. Good numbers of converted photons and especially significantly fast scintillation response compared with commercial NaI:Tl could be propitious in low-cost and large-size scintillator fabrication. Moreover, we successfully employed our Li-(PEA)₂PbBr₄ scintillator in alpha particle detection and in discrimination between alpha particle and gamma-ray. Based on the thermal neutron results for crystals doping with natural Li and ⁶Li, our Li-doped crystal will be a promising thermal neutron scintillator provided more ⁶Li is included as it is low cost and it can be deposited in large-area arrays of photodetectors. Finally, we carried out low-dose X-ray imaging using high-quality Li-(PEA)₂PbBr₄ film prepared by our new technique and obtained first satisfactory X-ray imaging pictures using (PEA)₂PbBr₄ perovskite to our knowledge. Here we show promising characterization results and prove that our Li-(PEA)₂PbBr₄ scintillator may hold promise as a low-cost and versatile radiation detector covering a wide range of energy from keV up to MeV.

Methods

Li-(PEA)₂PbBr₄ crystals and film preparation. Dimethyl sulfoxide (DMSO, anhydrous), phenethylammonium bromide (PEA)Br, 98%, lead bromide (PbBr₂, 98%), and lithium bromide (LiBr, ≥99%) were purchased from Sigma-Aldrich. Undoped precursor solution was prepared by dissolving equal molar amount of (PEA)Br and PbBr₂ in DMSO under stirring at 100 °C for 2 h under N₂. Crystals were obtained by evaporating DMSO from 3 M precursor solution in ambient environment slowly; it could take a few weeks. The crystal precipitate was then washed with diethyl ether and dried under vacuum for future characterizations. For Li-(PEA)₂PbBr₄ crystals, the procedure was the same as that of the undoped one except for the addition of LiBr to the precursor solution. The amount of LiBr depends on the molar ratio between Li and Pb. In our experiment, one undoped and three doping concentration were prepared, i.e., molar ratio Li:Pb = 0, 1:100, 1:10, and 1:1 (denoted as undoped, 1:100, 1:10, and 1:1). The concentration of the precursor solution is 3 M except 1:1 Li-(PEA)₂PbBr₄ (2 M due to limited solubility of LiBr). Here, it should be noted that the ratio is from the precursor instead of the final product. For the film preparation, precursor solution (1:1, 2 M concentration for high viscosity) was spin-coated on a UV-ozone treated cover glass substrate with 500 rpm for 60 s (acceleration: 100 rpm per s). In the last 30 s, a heat gun was applied right on top of the film to blow-dry the film with hot air flow. The film was baked at 100 °C on a hot plate for another 20 min.

Structure and composition characterization. The structure was determined by powder X-ray diffraction (XRD) measurement. The XRD measurements were carried out on a Bruker D8 Discover with Cu Kα radiation (λ = 1.54 Å). Step increment and acquisition time were 0.05° and 1 s, respectively. The element composition was determined by X-ray photoemission spectroscopy (XPS) and inductively coupled plasma mass spectrometer (ICPMS) measurement. XPS measurements were performed in an integrated VG ESCA Lab system using an X-ray source of Magnesium Kα with typical excitation energy output of 1254 eV. The entire experiments were carried out in an ultrahigh vacuum (UHV) system with typical base pressure in the range of ~10⁻¹⁰ mbar and the whole acquisition data were taken at room temperature. The impinged spot size on the sample is about

1 mm in diameter. ICPMS samples were prepared by dissolving respective crystals in deionized water (18 MΩ) and the ICPMS equipment model was PerkinElmer ELAN DRC-e.

Temperature-dependent X-ray luminescence measurement. The experiment was carried out in a similar way as our previous one³¹. A typical setup consisting of an Inel XRG3500 X-ray generator (Cu-anode tube, 45 kV/10 mA), an Acton Research Corporation SpectraPro-500i monochromator (500 nm blazed grating), a Hamamatsu R928 photomultiplier, and an APD Cryogenics Inc. closed-cycle helium cooler with a Lake Shore 330 programmable temperature controller was used to record XL spectra at various temperatures between 10 and 350 K. The measurements were carried out starting at 350 K (unless indicated) and terminating at 10 K to avoid a possible contribution from thermal release of charge carriers to the emission yield.

X-ray thermoluminescence (TL) measurement. The same setup was used as the one in temperature-dependent X-ray luminescence measurement. Prior to the TL runs, the sample was exposed for 10 min to X-ray at about 10 K. The glow curve was recorded up to 350 K at a heating rate of about 0.14 K per s.

Gamma-ray pulse height and excited decay measurement. We used ¹³⁷Cs (662 KeV) radioisotope for gamma-ray source and various photomultipliers (PMT) (Hamamatsu R2059, Hamamatsu R878, and Photonis XP Series) for detecting the converted photons. To operate the PMT, we applied a voltage between 1.25 and 1.7 kV. The corresponding output signal from PMT is integrated with a charge sensitive pre-amplifier. The output then feeds a spectroscopic amplifier with a shaping time of 2 μs and an analog-to-digital converter (Ortec series). The photoelectron yield was obtained by comparing the position of photopeak to the position of the mean value of the single electron response in pulse high spectra measurements. The actual light yield for the radiation conversion in photons per MeV was obtained after the photoelectron yield was divided by the quantum efficiencies of the PMT. Scintillation decay measurements were performed by the delayed coincidence single photon counting method, originally proposed by Bollinger and Thomas⁵⁶. A ¹³⁷Cs radioactive source, two Hamamatsu photomultiplier tubes (R1104 and R928 for “starts” and “stops”, respectively), a Canberra 2145 time-to-amplitude converter, and a TUKAN-8K-USB multichannel analyzer were used.

Alpha particle pulse-height measurement. Four alpha-emitting sources were used: ²⁴¹Am (5486 keV), ²⁴⁴Cm (5805 keV), ²²⁸Th (with progeny ²¹²Po: 8785 keV), ²³⁰Th (4687 keV). To perform alpha particle spectroscopy, the crystal was mounted on the window of a Hamamatsu R9880U-20 photomultiplier tube (PMT), with a thin layer of silicone grease to provide optical coupling. This PMT has a fast time response (0.6 ns rise time), a broad spectral sensitivity (230–920 nm), and an 8-mm diameter photocathode sensitive area. The PMT was operated at a voltage of ~750 V for these measurements. The PMT anode signal was input directly to a Caen DT5720D digital pulse processing (DPP) unit which integrated the anode charge pulses over a 92 ns gate. Caen’s COMPASS software was used to control the DPP parameters and accumulate pulse-height (proportional to energy) spectra for each radioactive source. These radioactive sources were positioned (in air) at 2 mm distance from the surface of the crystal. More detail can be found in Supplementary Information.

Pulse-shape discrimination (PSD) between alpha particle and gamma ray. The PSD capability of 1:1 Li-(PEA)₂PbBr₄ crystal was tested under alpha particle and gamma-ray signals using ¹³⁷Cs and ²⁴¹Am source, respectively. The crystal was mounted on a Hamamatsu multiplier tube R6233-100 and covered with several Teflon layers, except a small hole was opened to enable alpha particle irradiation. The PMT anode signal was digitized directly by a fast analog-to-digital converter (FADC400 Notice Korea) with recording length of 2.56 μs for each pulse. A ROOT-based C++ program was used to record data to a Linux-based PC used for

further analysis. The optimum filter method was employed for PSD study with detail information can be found in this reference⁵⁷.

X-ray imaging setup. The X-ray source was PHYWE XR 4.0 expert unit (Cu anode, 35 kV, 1 mA) and the camera was Chameleon CMLN-13S2C (exposure time depends on varied samples, usually 1–3 s). The equipment was placed as shown in the scheme in Fig. 6a. The envelop with the safety pin inside was put at the aperture of the X-ray tube where the uncollimated X-ray came out. The envelop, the perovskite film and the camera were placed as close as possible to reduce light scattering.

Data availability

The data that support the results presented in the paper are available from the corresponding authors upon reasonable request.

Received: 6 February 2020; Accepted: 21 May 2020;

Published online: 24 June 2020

References

- Yakunin, S. et al. Detection of X-ray photons by solution-processed lead halide perovskites. *Nat. Photonics* **9**, 444–449 (2015).
- Büchle, P. et al. X-ray imaging with scintillator-sensitized hybrid organic photodetectors. *Nat. Photonics* **9**, 843–848 (2015).
- Wei, H. et al. Sensitive X-ray detectors made of methylammonium lead tribromide perovskite single crystals. *Nat. Photonics* **10**, 333–339 (2016).
- Yakunin, S. et al. Detection of gamma photons using solution-grown single crystals of hybrid lead halide perovskites. *Nat. Photonics* **10**, 585 (2016).
- Kishimoto, S. et al. Subnanosecond time-resolved X-ray measurements using an organic-inorganic perovskite scintillator. *Appl. Phys. Lett.* **93**, 261901 (2008).
- Eijk, C. W. E. V. Inorganic scintillators in medical imaging. *Phys. Med. Biol.* **47**, R85–R106 (2002).
- Dujardin, C. et al. Needs, trends, and advances in inorganic scintillators. *IEEE Trans. Nucl. Sci.* **65**, 1977–1997 (2018).
- Weber, M. J. Inorganic scintillators: today and tomorrow. *J. Lumin.* **100**, 35–45 (2002).
- Yang, S. et al. Organohalide lead perovskites: more stable than glass under gamma-ray radiation. *Adv. Mater.* **0**, 1805547 (2018).
- Bokdam, M. et al. Role of polar phonons in the photo excited state of metal halide perovskites. *Sci. Rep.* **6**, 28618 (2016).
- Blancon, J. C. et al. Scaling law for excitons in 2D perovskite quantum wells. *Nat. Commun.* **9**, 2254 (2018).
- Chen, Q. et al. All-inorganic perovskite nanocrystal scintillators. *Nature* **561**, 83–88 (2018).
- Zhang, Y. et al. Metal halide perovskite nanosheet for X-ray high-resolution scintillation imaging screens. *ACS Nano* **13**, 2520–2525 (2019).
- Wei, H. et al. Dopant compensation in alloyed $\text{CH}_3\text{NH}_3\text{PbBr}_{3-x}\text{Cl}_x$ perovskite single crystals for gamma-ray spectroscopy. *Nat. Mater.* **16**, 826–833 (2017).
- Shakti, N., Devi, C., Patra, A. K., Gupta, P. S. & Kumar, S. Lithium doping and photoluminescence properties of ZnO nanorods. *AIP Adv.* **8**, 015306 (2018).
- Fang, Z., He, H., Gan, L., Li, J. & Ye, Z. Understanding the role of lithium doping in reducing nonradiative loss in lead halide perovskites. *Adv. Sci.* **5**, 1800736 (2018).
- Jiang, Q. et al. Electrochemical doping of halide perovskites with ion intercalation. *ACS Nano* **11**, 1073–1079 (2017).
- Bollinger, L. M., Thomas, G. E. & Ginther, R. J. Neutron detection with glass scintillators. *Nucl. Instrum. Methods* **17**, 97–116 (1962).
- Clifford, E. T. H. et al. A militarily fielded thermal neutron activation sensor for landmine detection. *Nucl. Instrum. Methods Phys. Res., Sect. A* **579**, 418–425 (2007).
- Wu, W., Tong, M., Xiao, L. & Wang, J. Porosity sensitivity study of the compensated neutron logging tool. *J. Pet. Sci. Eng.* **108**, 10–13 (2013).
- Chica, D. G. et al. Direct thermal neutron detection by the 2D semiconductor ${}^6\text{LiInP}_2\text{Se}_6$. *Nature* **577**, 346–349 (2020).
- Kumar, S. et al. Efficient blue electroluminescence using quantum-confined two-dimensional perovskites. *ACS Nano* **10**, 9720–9729 (2016).
- Birowsuto, M. D. et al. X-ray scintillation in lead halide perovskite crystals. *Sci. Rep.* **6**, 37254 (2016).
- Jia, G. et al. Super air stable quasi-2D organic-inorganic hybrid perovskites for visible light-emitting diodes. *Opt. Express* **26**, A66–A74 (2018).
- Kawano, N. et al. Scintillating organic-inorganic layered perovskite-type compounds and the gamma-ray detection capabilities. *Sci. Rep.* **7**, 14754 (2017).
- Yang, B. et al. Lead-free halide Rb_2CuBr_3 as sensitive X-ray scintillator. *Adv. Mater.* **31**, 1904711 (2019).
- Shibuya, K., Koshimizu, M., Nishikido, F., Saito, H. & Kishimoto, S. Poly[bis(phenethylammonium) [dibromodiplumbate(ii)]-di-[μ]-bromido]]. *Acta Crystallogr., Sect. E: Crystallogr. Commun.* **65**, m1323–m1324 (2009).
- Peng, B. et al. Bose–einstein oscillators and the excitation mechanism of free excitons in 2D layered organic-inorganic perovskites. *RSC Adv.* **7**, 18366–18373 (2017).
- Smith, M. D., Jaffe, A., Dohner, E. R., Lindenberg, A. M. & Karunadasa, H. I. Structural origins of broadband emission from layered Pb–Br hybrid perovskites. *Chem. Sci.* **8**, 4497–4504 (2017).
- Yu, J. et al. Broadband extrinsic self-trapped exciton emission in Sn-doped 2D lead-halide perovskites. *Adv. Mater.* **31**, 1806385 (2019).
- Xie, A. et al. Thermal quenching and dose studies of X-ray luminescence in single crystals of halide perovskites. *J. Phys. Chem. C* **122**, 16265–16273 (2018).
- Hajime, S. Negative thermal quenching curves in photoluminescence of solids. *Jpn. J. Appl. Phys.* **37**, 550 (1998).
- Zhai, W. et al. Acetone vapour-assisted growth of 2D single-crystalline organic lead halide perovskite microplates and their temperature-enhanced photoluminescence. *RSC Adv.* **8**, 14527–14531 (2018).
- Cui, X. et al. Temperature-dependent electronic properties of inorganic-organic hybrid halide perovskite ($\text{CH}_3\text{NH}_3\text{PbBr}_3$) single crystal. *Appl. Phys. Lett.* **111**, 233302 (2017).
- Li, J. et al. Temperature-dependent photoluminescence of inorganic perovskite nanocrystal films. *RSC Adv.* **6**, 78311–78316 (2016).
- Yangui, A. et al. Optical investigation of broadband white-light emission in self-assembled organic-inorganic perovskite ($\text{C}_6\text{H}_{11}\text{NH}_3$) $_2\text{PbBr}_4$. *J. Phys. Chem. C* **119**, 23638–23647 (2015).
- Randall, J. T., Wilkins, M. H. F. & Oliphant, M. L. E. Phosphorescence and electron traps II. The interpretation of long-period phosphorescence. *Proc. R. Soc. Lond. A* **184**, 347–364 (1945).
- Eijk, C. W. E. V. et al. Scintillation properties of a crystal of ($\text{C}_6\text{H}_5(\text{CH}_2)_2\text{NH}_3$) $_2\text{PbBr}_4$. In *2008 IEEE Nuclear Science Symposium Conference Record* 3525–3528 (IEEE, 2008).
- Saidaminov, M. I. et al. High-quality bulk hybrid perovskite single crystals within minutes by inverse temperature crystallization. *Nat. Commun.* **6**, 7586 (2015).
- de Haas, J. T. M., Dorenbos, P. & van Eijk, C. W. E. Measuring the absolute light yield of scintillators. *Nucl. Instrum. Methods Phys. Res., Sect. A* **537**, 97–100 (2005).
- Dorenbos, P., Haas, J. T. M. D. & Eijk, C. W. E. V. Non-proportionality in the scintillation response and the energy resolution obtainable with scintillation crystals. *IEEE Trans. Nucl. Sci.* **42**, 2190–2202 (1995).
- Birowsuto, M. D. *Novel Gamma-ray and Thermal-neutron Scintillators: Search for High-light-yield and Fast-response Materials* (IOS Press, 2008).
- McCall, K. M. et al. α -particle detection and charge transport characteristics in the $\text{A}_3\text{M}_2\text{I}_9$ defect perovskites (A = Cs, Rb; M = Bi, Sb). *ACS Photonics* **5**, 3748–3762 (2018).
- Mykhaylyk, V. B., Kraus, H. & Saliba, M. Bright and fast scintillation of organolead perovskite MAPbBr $_3$ at low temperatures. *Mater. Horiz.* **6**, 1740–1747 (2019).
- He, Y. et al. Perovskite CsPbBr $_3$ single crystal detector for alpha-particle spectroscopy. *Nucl. Instrum. Methods Phys. Res., Sect. A* **922**, 217–221 (2019).
- Knoll, G. F. *Radiation Detection and Measurement* 3rd edn (Wiley, 1989).
- Minami, Y. et al. Spectroscopic investigation of praseodymium and cerium Co-doped 20Al(PO $_3$) $_3$ -80LiF glass for potential scintillator applications. *J. Non-Cryst. Solids* **521**, 119495 (2019).
- Gatti, E. & Martini, F. D. *Nuclear Electronics* Vol. 2, 265–276 (Brueder Rosenbaum, 1962).
- Roush, M. L., Wilson, M. A. & Hornyak, W. F. Pulse shape discrimination. *Nucl. Instrum. Methods* **31**, 112–124 (1964).
- Yamazaki, A. et al. Neutron-gamma discrimination based on pulse shape discrimination in a Ce:LiCaAlF $_6$ scintillator. *Nucl. Instrum. Methods Phys. Res., Sect. A* **652**, 435–438 (2011).
- Birowsuto, M. D. et al. Thermal-neutron scintillator: Ce $^{3+}$ activated Rb $_2$ LiYBr $_6$. *J. Appl. Phys.* **101**, 066107 (2007).
- Guss, P., Stampahar, T., Mukhopadhyay, S., Barzilov, A. & Guckes, A. Scintillation properties of a Cs $_2$ LiLa(Br $_6$) $_9$ 0%Cl $_6$ 10%Ce $^{3+}$ (CLLC) crystal. In *Radiation Detectors: Systems and Applications XV*. Vol. 9215 (SPIE, 2014).
- Birowsuto, M. D. et al. Li-based thermal neutron scintillator research: Rb $_2$ LiYBr $_6$:Ce $^{3+}$ and other elpasolites. *IEEE Trans. Nucl. Sci.* **55**, 1152–1155 (2008).
- NIST. *XCOM Calculator*, <https://www.physics.nist.gov/PhysRefData/Xcom/html/xcom1.html> (2010).
- Ng, Y. F. et al. Rapid crystallization of all-inorganic CsPbBr $_3$ perovskite for high-brightness light-emitting diodes. *ACS Omega* **2**, 2757–2764 (2017).
- Bollinger, L. M. & Thomas, G. E. Measurement of the time dependence of scintillation intensity by a delayed-coincidence method. *Rev. Sci. Instrum.* **32**, 1044–1050 (1961).

57. Vuong, P. Q., Kim, H., Park, H., Rooh, G. & Kim, S. Pulse shape discrimination study with Ti_2ZrCl_6 crystal scintillator. *Radiat. Meas.* **123**, 83–87 (2019).
58. Momma, K. & Izumi, F. Vesta: a three-dimensional visualization system for electronic and structural analysis. *J. Appl. Crystallogr* **41**, 653–658 (2008).
59. Momma, K. & Izumi, F. Vesta 3 for three-dimensional visualization of crystal, volumetric and morphology data. *J. Appl. Crystallogr* **44**, 1272–1276 (2011).

Acknowledgements

We would like to thank the financial support from Singapore Ministry of Education through AcRF Tier1 grant (MOE2017-T1-002-142). We also thank Dr. Philip Anthony Surman for proof reading and fruitful discussion about the paper.

Author contributions

M.D.B. and Cuong D. conceived the idea and supervised the project. A.X. performed the crystal synthesis, X-ray imaging, most of the data analysis, and paper writing. C.H. carried out the XRD measurement. F.M. contributed to the X-ray imaging. M.E.W., M.M., and W.D. contributed to the temperature-dependent X-ray luminescence, thermoluminescence, and gamma-ray characterizations. A. and A.T.S.W. performed the XPS measurement. S.V.S. carried out the alpha particle pulse-height measurement. P.Q.V. and H.J.K. contributed to the pulse-shape discrimination, thermal neutron measurements, and the related data analysis. Christophe D. and P.C. contributed to the data analysis. All authors contributed to the discussion and the writing of the paper.

Competing interests

The authors declare no competing interests.

Additional information

Supplementary information is available for this paper at <https://doi.org/10.1038/s43246-020-0038-x>.

Correspondence and requests for materials should be addressed to M.D.B. or C.D.

Reprints and permission information is available at <http://www.nature.com/reprints>

Publisher's note Springer Nature remains neutral with regard to jurisdictional claims in published maps and institutional affiliations.



Open Access This article is licensed under a Creative Commons Attribution 4.0 International License, which permits use, sharing, adaptation, distribution and reproduction in any medium or format, as long as you give appropriate credit to the original author(s) and the source, provide a link to the Creative Commons license, and indicate if changes were made. The images or other third party material in this article are included in the article's Creative Commons license, unless indicated otherwise in a credit line to the material. If material is not included in the article's Creative Commons license and your intended use is not permitted by statutory regulation or exceeds the permitted use, you will need to obtain permission directly from the copyright holder. To view a copy of this license, visit <http://creativecommons.org/licenses/by/4.0/>.

© The Author(s) 2020

Supplementary Information

Lithium-doped two-dimensional perovskite scintillator for wide-range radiation detection

Aozhen Xie^{1,2}, Chathuranga Hettiarachchi², Francesco Maddalena¹, Marcin E. Witkowski³, Michał Makowski³, Winicjusz Drozdowski³, Arramel⁴, Andrew T. S. Wee⁴, Stuart Victor Springham⁵, Phan Quoc Vuong⁶, Hong Joo Kim⁶, Christophe Dujardin⁷, Philippe Coquet^{1,2,8}, Muhammad Danang Birowosuto^{1,2} & Cuong Dang^{1,2}

¹CINTRA UMI CNRS/NTU/THALES 3288, Research Techno Plaza, 50 Nanyang Drive, Border X Block, Level 6, Singapore 637553 Singapore

²School of Electrical and Electronics Engineering, Nanyang Technological University, 50 Nanyang Avenue, Singapore 639798, Singapore

³Institute of Physics, Faculty of Physics, Astronomy, and Informatics, Nicolaus Copernicus University in Torun, ul. Grudziadzka 5, Torun 87-100, Poland

⁴Department of Physics, National University of Singapore, 2 Science Drive 3, 117542, Singapore

⁵Natural Sciences and Science Education, National Institute of Education, 637616, Singapore

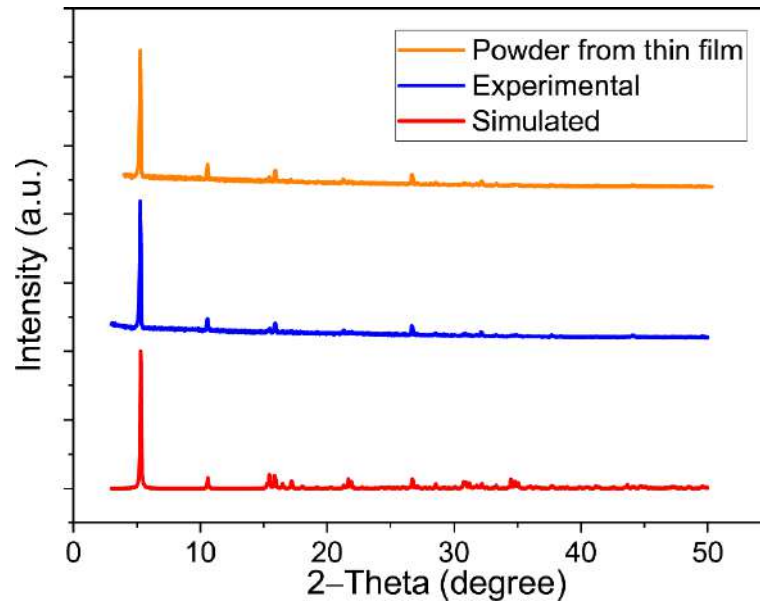
⁶Department of Physics, Kyungpook National University, Daegu 41566, Korea

⁷Université de Lyon, Université Claude Bernard, Lyon 1, CNRS, Institut Lumière Matière UMR5306, Villeurbanne F-69622, France

⁸Institut d'Electronique, de Microélectronique et de Nanotechnologie (IEMN), CNRS UMR 8520- Université de Lille, Villeneuve d'Ascq 59650, France

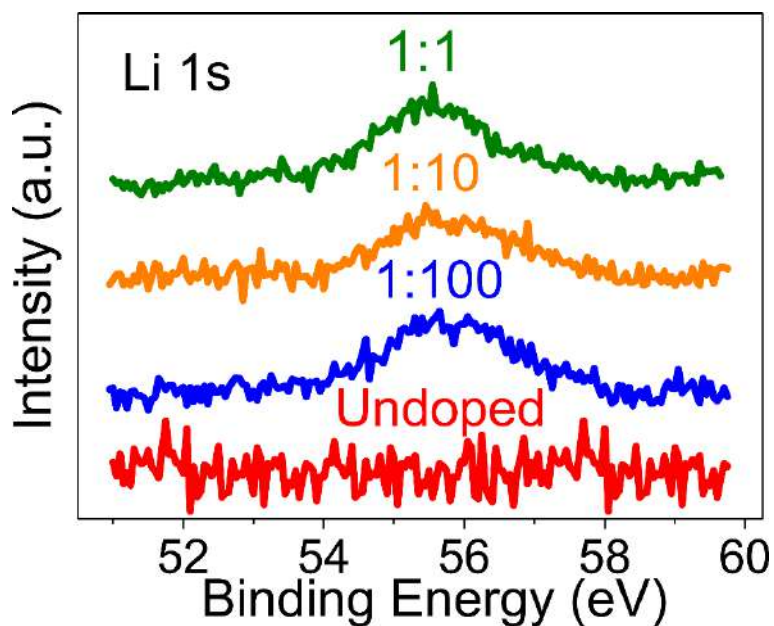
Correspondence and requests for materials should be addressed to M.D.B. (mbirowosuto@ntu.edu.sg) or C.D. (hcdang@ntu.edu.sg)

Powder X-ray diffraction (XRD).



Supplementary Figure 1. Comparison of experimental and simulated powder XRD pattern of undoped (PEA)₂PbBr₄. The experimental curve is from single crystal powder. Thin film powder curve is also included to demonstrate that there is little change of crystal phase after spin-coating. The simulated result is based on the crystallographic information file reported by Shibuya¹. The characteristics of XRD peaks from our crystal match well with the simulation.

Li concentration from XPS and ICPMS measurements.



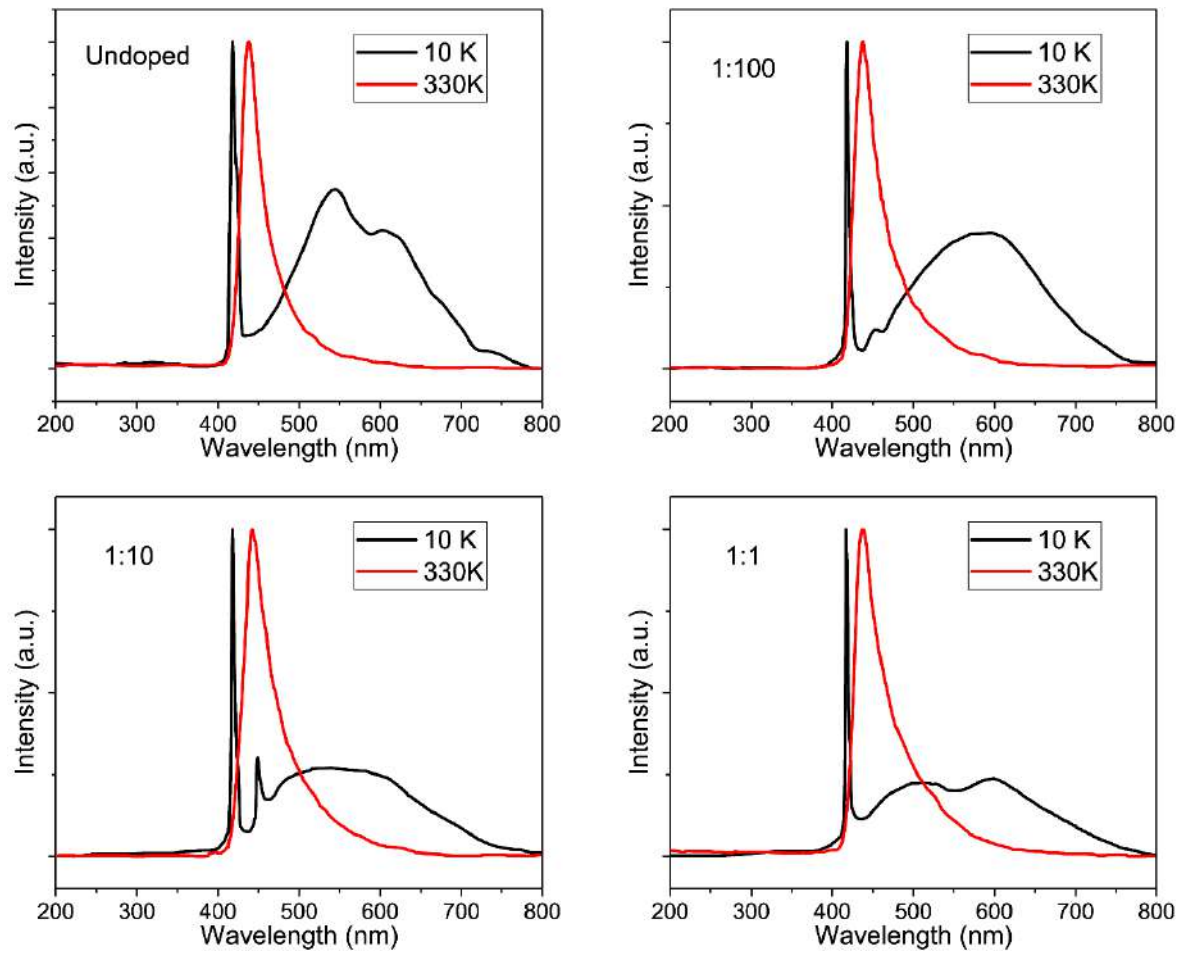
Supplementary Figure 2. Li 1s XPS signals that have been normalized to respective Pb 4f signals. It reflects the slow increase of Li in the doped crystals though the large amount of Li dopant was added in the precursor solutions.

Supplementary Table 1 Result of ICPMS to estimate Li/Pb ratio of the all crystals.

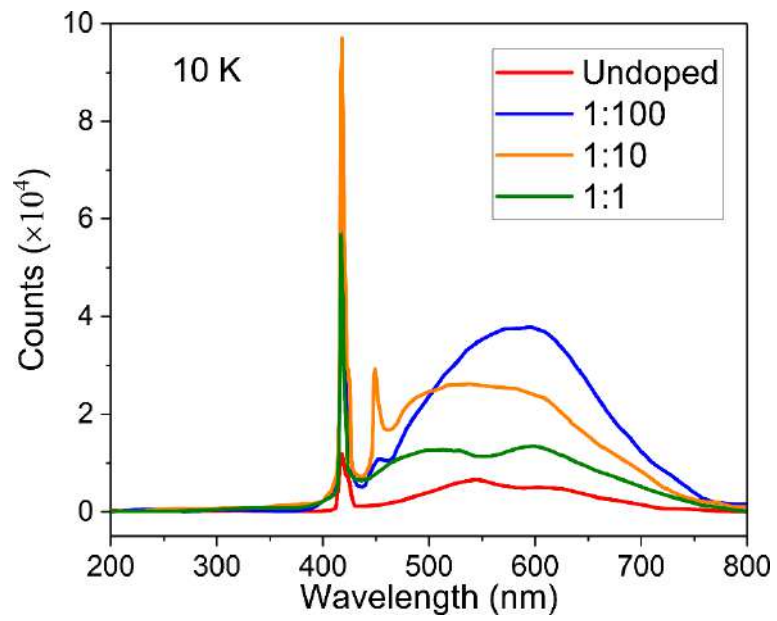
Li/Pb precursor ratio	Li concentration (ppb)	Pb concentration (ppb)	Li:Pb sample ratio (%)
Undoped	1.74	11600	0%
1:100	2.22	150	1%
1:10	3.31	146	2%
1:1	6.99	160	4%

The ICPMS result agrees well with the XPS result, where an estimation of 5% Li:Pb sample ratio from XPS signal integration.

Comparison of XL.

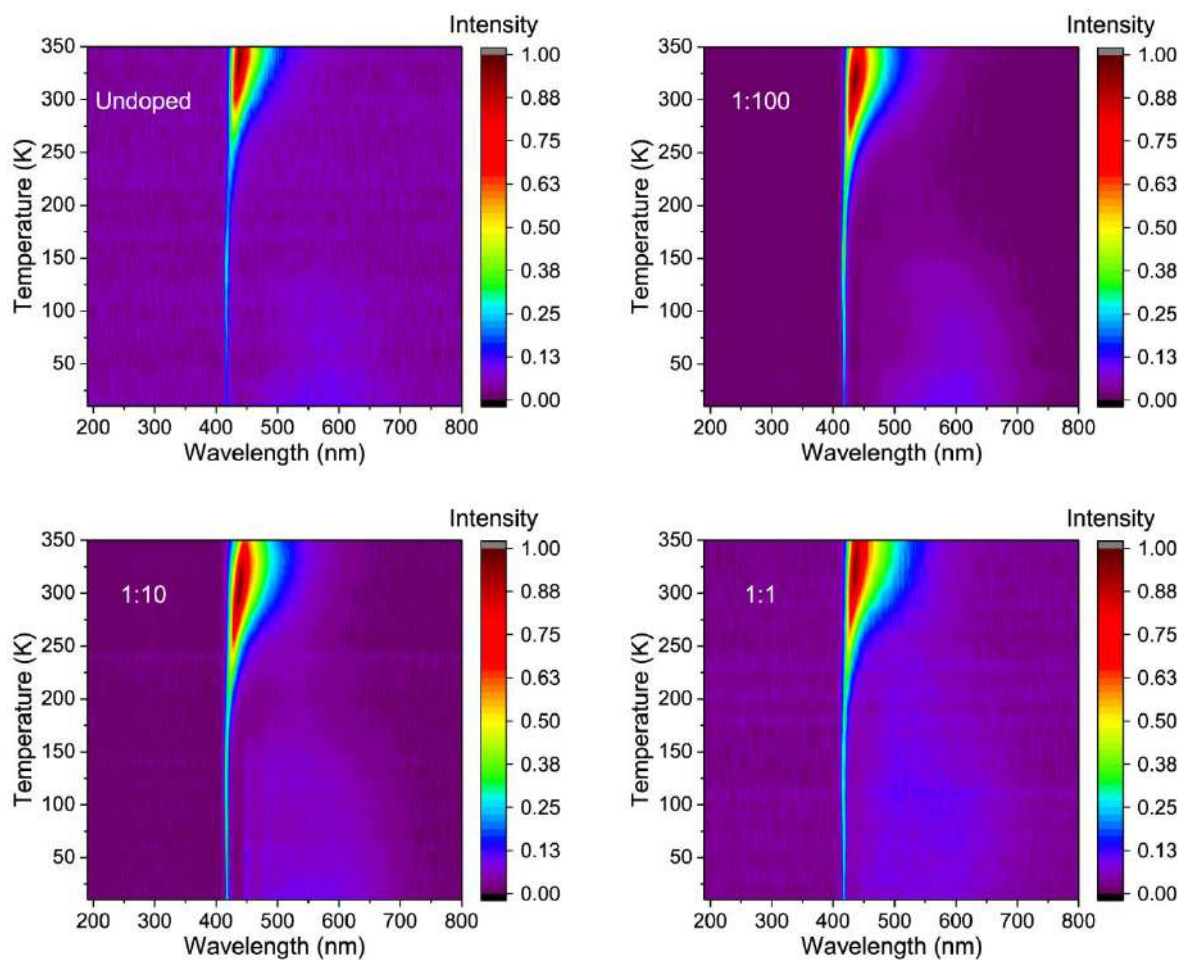


Supplementary Figure 3. Comparison of normalized XL spectra between 10 K and 330 K from undoped, 1:100, 1:10 and 1:1 Li-doped crystals. At 10 K, all four crystals show STE emissions after the FE emissions. The STE emissions seem to be affected by Li dopant concentration. In addition, we can see the tendency of FE emission broadening.



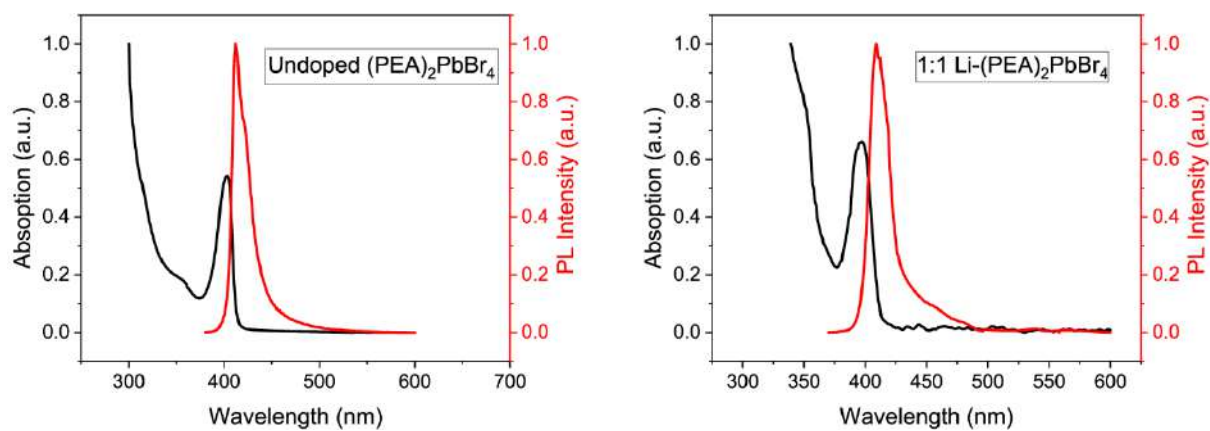
Supplementary Figure 4. Comparison of XL at 10 K. The absolute emission counts of Li-doped crystals are all higher than undoped one.

Comparison of 2D XL map.



Supplementary Figure 5. Comparison of temperature-dependent 2D map from undoped, 1:100, 1:10 and 1:1 Li-doped crystals. The tendency of emission broadening is apparent from undoped to highest-doped crystal. Negative thermal quenching can be observed as well.

UV-Vis absorption and photoluminescence spectra comparison of undoped and 1:1 Li-doped $(\text{PEA})_2\text{PbBr}_4$.



Supplementary Figure 6. UV-Vis absorption and PL excited by 360 nm UV in ambient. There is an overlap in the absorption and emission at around 410 nm, which induces the reabsorption at this overlapped region. It follows that the emission peak is asymmetric and sharp at the lower wavelength.

Supplementary Discussion 1. Negative thermal quenching behaviour analysis.

In this case, we can apply the model in the simplest case,

$$I(T)_{norm} = \frac{1 + D \exp(-E'_1/k_B T)}{1 + C \exp(-E_1/k_B T)} \quad (1)$$

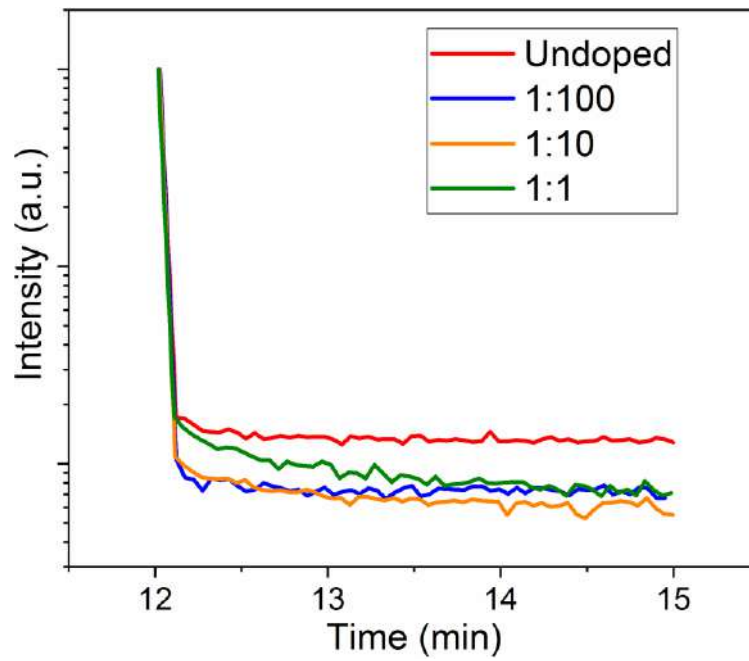
where $I(T)_{norm}$ is the integrated emission intensity at absolute temperature T normalized to the maximum integrated intensity, D is the negative thermal quenching coefficient which describes the contribution from thermally excited electrons, C is the thermal quenching coefficient related to non-radiative electron excitation, E'_1 and E_1 are the activation energies for negative thermal quenching and typical thermal quenching and k_B is the Boltzmann constant. The fitting parameters are listed in Supplementary Table 2.

Supplementary Table 2. Parameters of negative thermal quenching.

Item	D	C	E'_1 (meV)	E_1 (meV)
Undoped	$6.69 \cdot 10^5$	$2.46 \cdot 10^6$	4.38	4.30
Li:Pb = 1:100	$5.82 \cdot 10^6$	$1.28 \cdot 10^7$	5.33	5.07
Li:Pb = 1:10	$9.05 \cdot 10^5$	$2.04 \cdot 10^6$	4.85	4.69
Li:Pb = 1:1	$3.01 \cdot 10^6$	$5.93 \cdot 10^6$	4.87	4.87

As can be seen in Supplementary Table 2, values of D , C , E'_1 and E_1 from all crystals are very close. A slight increase in all parameters from undoped to highest doping crystals except 1:100. We admit that in our case for 1:100 and 1:10 crystals, the strongest emissions are at 350 K and we assume in the fitting the maximums are at 350 K, which in fact might not hold true if temperature goes above 350 K. Thus, it can affect to our fitting accuracy.

X-ray thermoluminescence spectra.



Supplementary Figure 7. Zoom-in TL spectra show the increasing afterglow upon higher Li concentration. The afterglow effect in undoped crystal is weaker than the other Li-doped ones and it is a result of traps generated by Li dopant.

Supplementary Table 3. Parameters of low-energy traps

Item	T_{max} (K)	E (meV)	n_0	s_i
Li:Pb = 1:100	37	10.8	$1.04 \cdot 10^5$	0.285
	78.5	41.74	$6.27 \cdot 10^4$	4.348
	120	124	$8.81 \cdot 10^4$	$1.87 \cdot 10^3$
Li:Pb = 1:10	39	10.8	$2.72 \cdot 10^5$	0.213
	78.5	41.74	$1.06 \cdot 10^5$	4.328
	117	123	$1.95 \cdot 10^5$	$2.83 \cdot 10^3$
Li:Pb = 1:1	45	10.8	$6.95 \cdot 10^5$	0.101
	78	41.74	$3.17 \cdot 10^5$	4.541
	114	124	$1.94 \cdot 10^5$	$4.11 \cdot 10^3$

Supplementary Discussion 2. Theoretical limit of energy resolution.²⁻⁴

Then energy resolution can be calculated by the following equation,

$$R^2 = \left(\frac{\Delta E}{E}\right)^2 = R_{np}^2 + R_{inh}^2 + R_p^2 + R_M^2 \quad (2)$$

where ΔE is the full width at half maximum of the total absorption peak in the gamma-ray pulse height spectrum, R_{np} is the contribution of the non-proportional response of the scintillator, R_{inh} is related to inhomogeneities of the scintillator, which causes fluctuations in the scintillation light yield, R_{inh} is connected to the fluctuation in the transfer efficiency, which results in the arrival of a photoelectron at the first dynode and subsequently undergoes the full multiplication in the PMT. R_M is determined by Poisson statistics in the number of detected photons N_{dph} , which is equal to the number of photoelectrons from the photocathode in case of a PMT. This resolution is also the fundamental limit for the energy resolution. It is given by

$$R_M = 2.35 \sqrt{\frac{1+v(M)}{N_{dph}}} \quad (3)$$

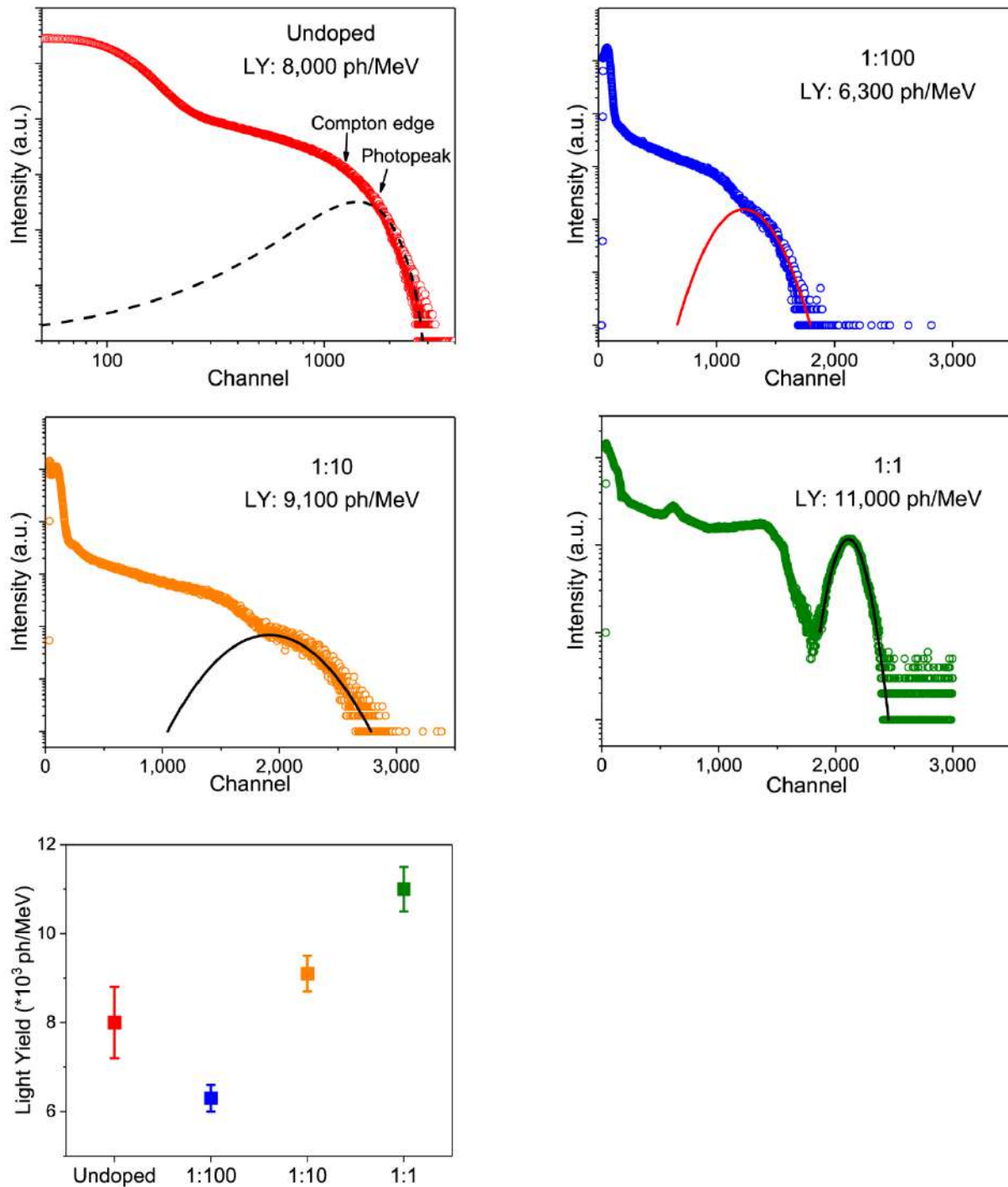
where $v(M)$ is the variance in the PMT gain which usually is 0.1-0.2. Theoretically, if the scintillator is a perfect one, then the first three terms can be neglected and the final term R_M is the only consideration while $v(M) = 0.1$. In this case,

$$R = R_M = 2.35 \sqrt{\frac{1+0.1}{N_{dph}}} \quad (4)$$

In our experiment, N_{dph} of 1:1 Li-(PEA)₂PbBr₄ is 1,655, the product of number of photoelectron/energy (2,500 phe/MeV) and the energy of the radiation source (0.662 MeV). After calculation of Eq. (4), we can obtain the theoretical limit of energy resolution,

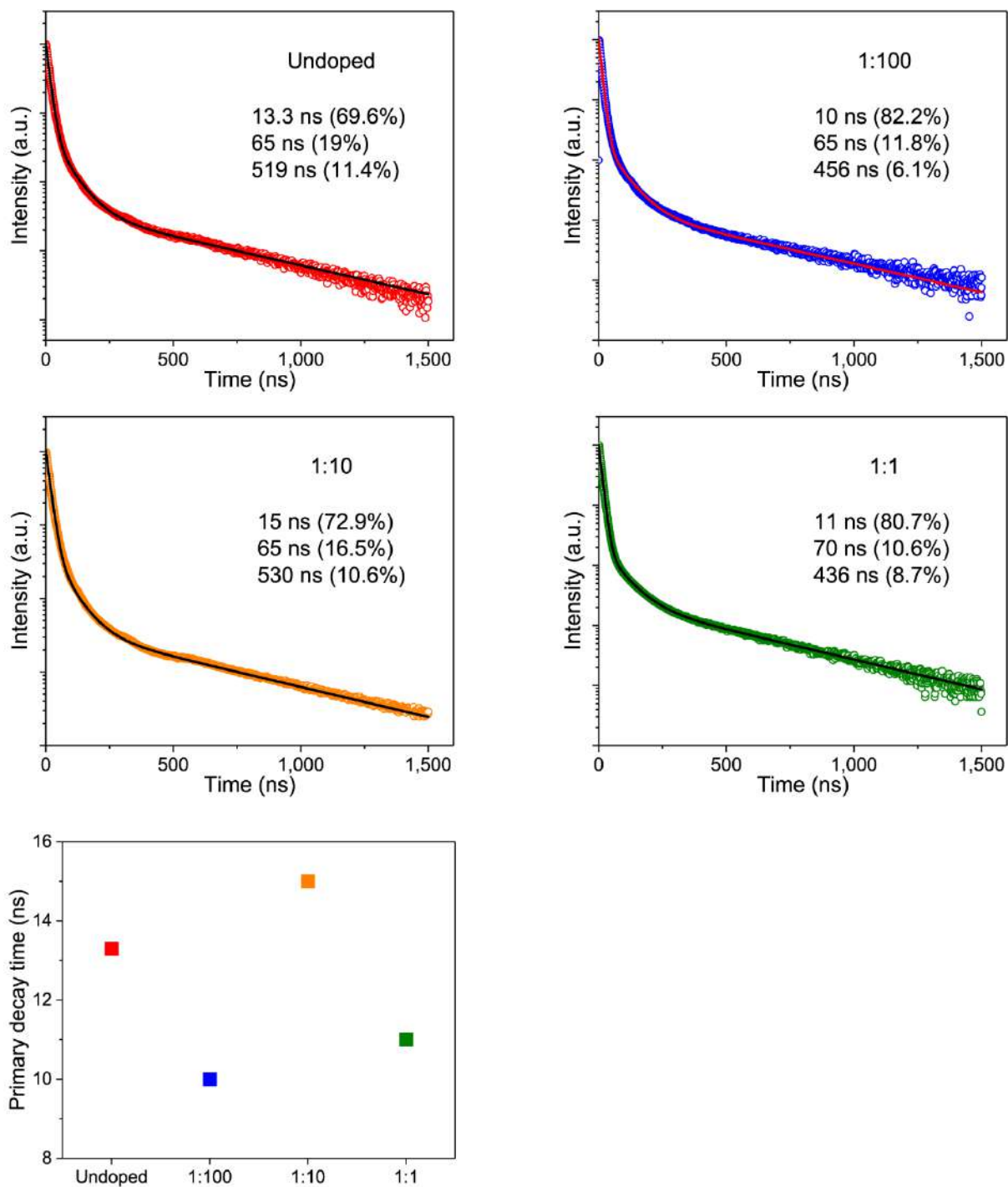
$$R = 6\%$$

Gamma-ray (^{137}Cs , 662 keV) pulse height and decay measurements.



Supplementary Figure 8. Gamma-ray pulse height measurements of undoped, 1:100, 1:10 and 1:1 Li-doped crystals. Gaussian fittings were employed to extract the light yields and energy resolutions. At the first glance, the photopeak of the undoped crystal seems indistinguishable as the others doped crystals so we put it in log-log scale. Its light yield and energy resolution are $8,000 \pm 800$ ph per MeV (based on the channel difference (~ 500 as shown in other figures) between the Compton edge

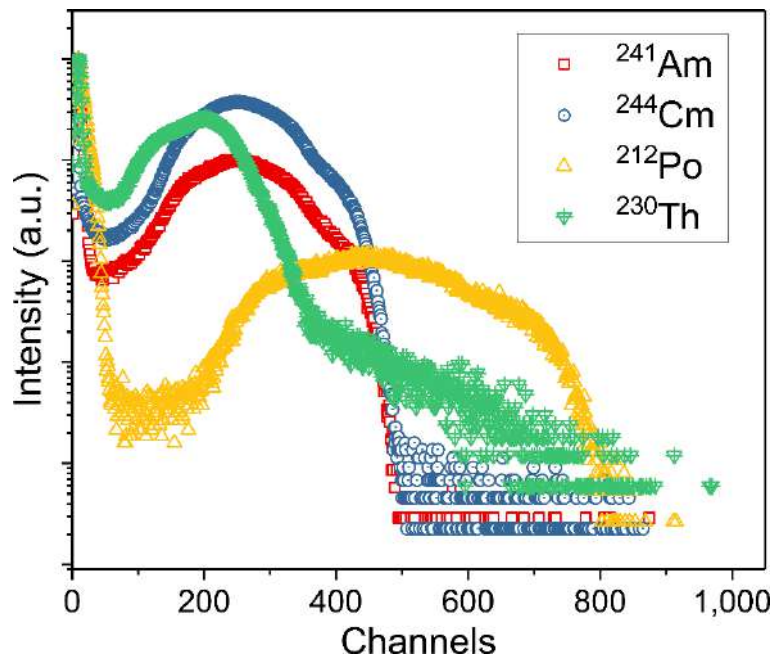
(1,100) and photopeak ($1,100 + 500 = 1,600$) and 55.4%, respectively. We also compare here our light yield result to early reports of undoped (PEA) 2PbBr_4 crystals (9,400 and 14,000 ph/MeV) although the characterization method might be different^{5,6}. In our experiments, the light yield increases as Li concentration increases from 1:100 to 1:1. The best energy resolution is from the highest 1:1 Li-doped crystal.



Supplementary Figure 9. Comparisons of gamma-ray excited decay of undoped, 1:100, 1:10 and 1:1 Li-doped crystals. Primary (fast) decay times from early reports are reported to be 9 and 11 ns^{5,6}.

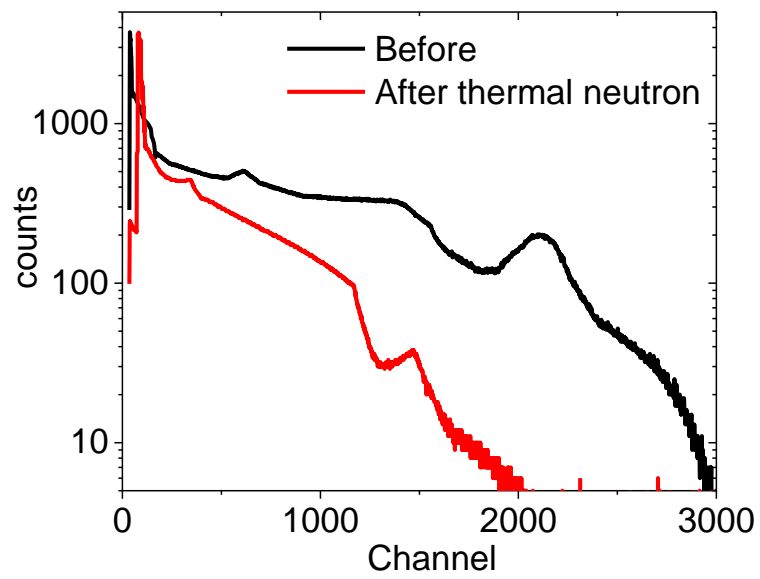
Alpha particle pulse height spectra.

Four alpha-emitting sources were used: ^{241}Am (5,486 keV), ^{244}Cm (5,805 keV), ^{228}Th (with progeny ^{212}Po : 8,785 keV), ^{230}Th (4,687 keV). However, the decay of ^{228}Th involves a chain of five alpha and two beta decays before stable ^{208}Pb is reached. Therefore, a time-coincidence technique was used to select pulses corresponding to the high energy 8785 keV alpha-particles from the decay of ^{212}Po (300 ns half-life). The beta decay of ^{212}Bi precedes the ^{212}Po alpha decay by a few hundred ns. List mode data was acquired by the DDP and pairs of pulses separated by less than 1 μs were selected; the second pulse of each pair was used to accumulate a pulse-height spectrum corresponding to alpha-particles emitted from ^{212}Po .



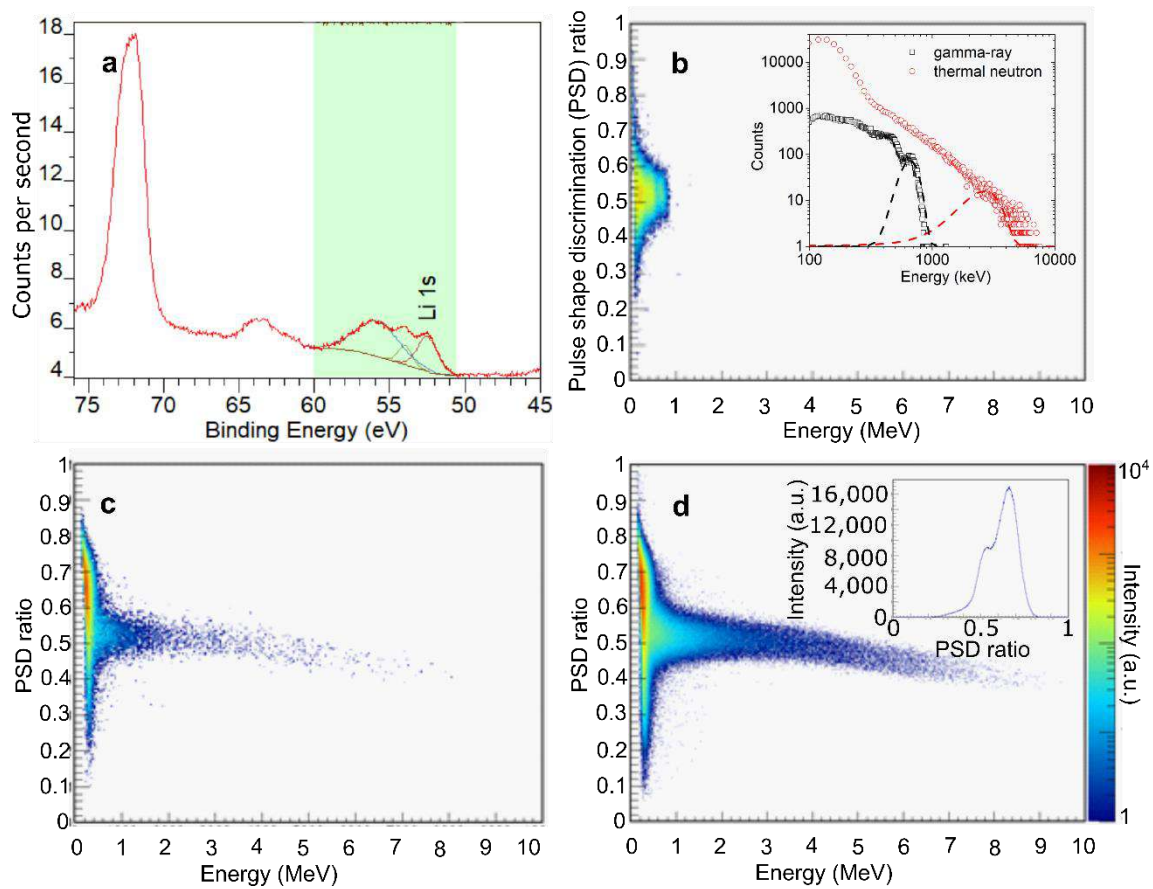
Supplementary Figure 10. Alpha particle pulse height spectra of ^{241}Am , ^{244}Cm , ^{212}Po and ^{230}Th . Relatively broad photopeaks corresponding to different radioisotopes can be discriminated. Poor energy resolution could be attributed to crystal morphology and inhomogeneity.

Radiation hardness.



Supplementary Figure 11. Pulse height spectra of ^{137}Cs measured before and after thermal neutron exposure of 4.8 MeV. The light yield drops from 10,500 to 7,000 ph per MeV after thermal neutron measurement while the energy resolution increases from 17.6 to 25.9.

X-ray photoelectron spectra of ${}^6\text{Li}$ and pulse shape discrimination between neutron and gamma-ray of preliminary enriched ${}^6\text{Li}$ -doped crystals.



Supplementary Figure 12. (a) X-ray photoelectron spectrum of 1:1 ${}^6\text{Li}$ -doped $(\text{PEA})_2\text{PbBr}_4$ crystal showing ${}^6\text{Li}$ peaks with binding energies between 52 and 56 eV. PSD matrix of 1 ${}^6\text{Li}$ doped crystals measured with (b) ${}^{137}\text{Cs}$ source, (c) 5-cm-organic glass moderated Am-Be neutrons source, and (d) direct neutron source. The insets in (b) and (d) exhibit the pulse height spectra with the gaussian fits and projection on y-axis for neutron signal, respectively. A huge number of events with PSD ratio centre at 0.66 observed for the neutron measurements is a clear evidence for neutron interaction with ${}^6\text{Li}$ doped crystals. Most neutrons are fast due to large amount of hydrogen in crystal. The figure of merit (FoM) based on PSD is expected to be 0.57. Theoretically, we have acceptable gamma rejection of 3-sigma (99.7%) with FoM of 1.27.

Supplementary Discussion 3. Calculation for thickness-dependent attenuation coefficient of 1:1 Li-(PEA)₂PbBr₄ with natural Li precursor and enriched ⁶Li precursor.

Here we assume atomic 5% Li/Pb LiBr dopant in 1:1 Li-(PEA)₂PbBr₄ crystal using XPS result and we calculated the difference in thickness-dependent attenuation coefficient.

Element	number of atoms n_i per molecule	Thermal neutron cross section σ_i (barn, 10^{-24} cm^{-2})	Total thermal neutron cross section (barn, 10^{-24} cm^{-2})
C	16	0.00353	0.05648
H	24	0.3326	7.9824
Br	4	6.9	35.535
N	2	1.9	3.8
Pb	1	0.171	0.171
⁶ Li	-	940	
⁷ Li	-	0.0454	
Natural Li precursor (7.59% ⁶ Li and 92.41% ⁷ Li)	0.05	70.5 ^a	3.525
Commercial enriched ⁷ Li precursor (95% ⁶ Li and 5% ⁷ Li)	0.05	893 ^a	44.65

a. Calculated from percentage averages of ⁶Li and ⁷Li.

The thermal neutron cross section of Li_{0.05}-(C₈H₁₂N)₂PbBr_{4.05} is the summation of the products of respective element cross sections σ_i and their number of atoms n .

For natural Li crystal (1:1)

$$\sigma_{\text{natural}} = \sum \sigma_i * n_i = 51.07 \text{ barn}$$

For enriched ${}^6\text{Li}$ crystal (1:1),

$$\sigma_{\text{enriched}} = \sum \sigma_i * n_i = 92.2 \text{ barn}$$

The theoretical detection efficiency maximum E is quotient of the cross section of Li dopant and the cross section of the molecule⁷,

$$E_{\text{natural}} = 3.525/51.07 = 7\%$$

$$E_{\text{enriched}} = 44.65/92.2 = 48\%$$

The number of molecule per unit volume N can be calculated by the density (ρ , 2.276 g/cm³), molecular weight (M_W , 771.19 g/mol) and the Avogadro constant (N_A , 6.02*10²³),

$$N = \rho / M_W * N_A = 2.276 / 771.19 * 6.02 * 10^{23} = 1.78 * 10^{21} \text{ cm}^{-3}$$

Macroscopic cross section (attenuation coefficient) Σ_{natural} and Σ_{enriched} are the product of number N and microscopic σ_{natural} and σ_{enriched} , respectively. Therefore, we have

$$\Sigma_{\text{natural}} = N * \sigma_{\text{natural}} = 0.09 \text{ cm}^{-1}$$

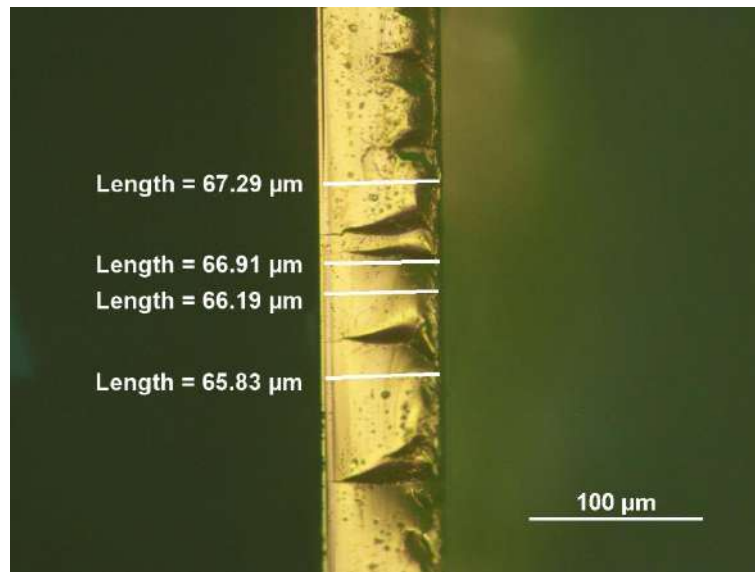
$$\Sigma_{\text{enriched}} = N * \sigma_{\text{enriched}} = 0.16 \text{ cm}^{-1}$$

The attenuation length L is,

$$L_{\text{natural}} = 1 / \Sigma_{\text{natural}} = 11 \text{ cm}$$

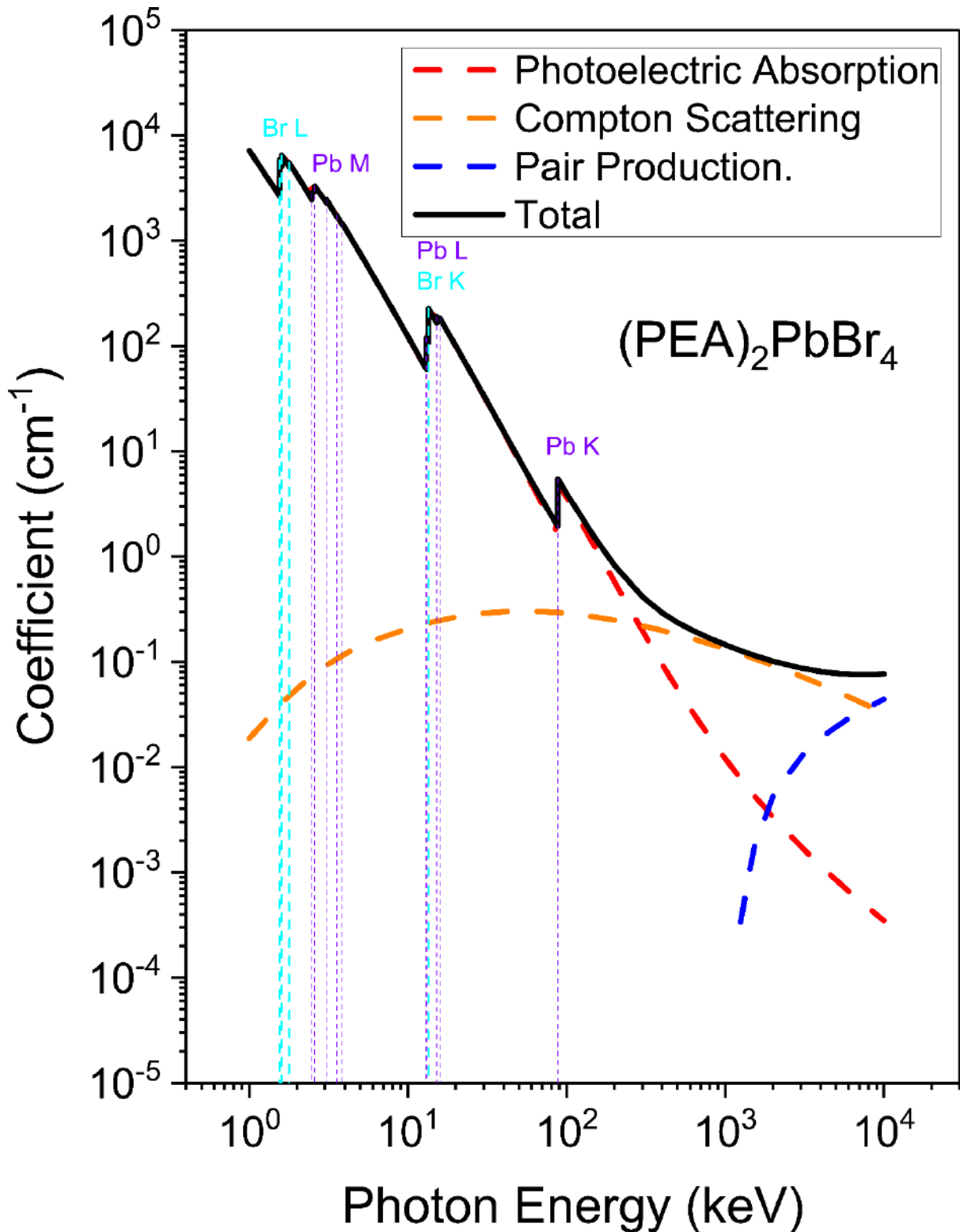
$$L_{\text{enriched}} = 1 / \Sigma_{\text{enriched}} = 6.1 \text{ cm}$$

1:1 Li-(PEA)₂PbBr₄ spin-coated film and X-ray imaging.



Supplementary Figure 13. Cross-section view of the spin-coated 1:1 Li-(PEA)₂PbBr₄ film (right) on a glass cover substrate (left). The thickness is around 67 μm . Flat surface of the film can be seen.

Supplementary Discussion 4. Thickness-dependent X-ray attenuation of $(\text{PEA})_2\text{PbBr}_4$ film.

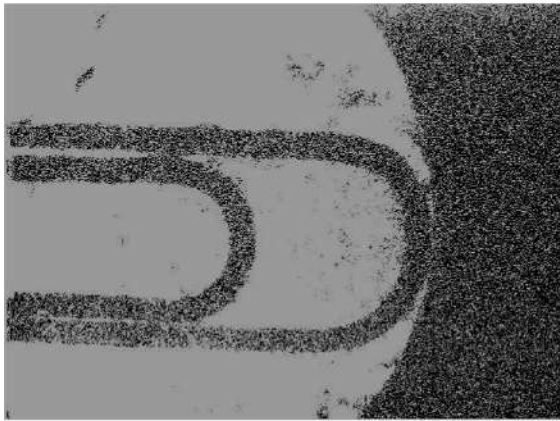
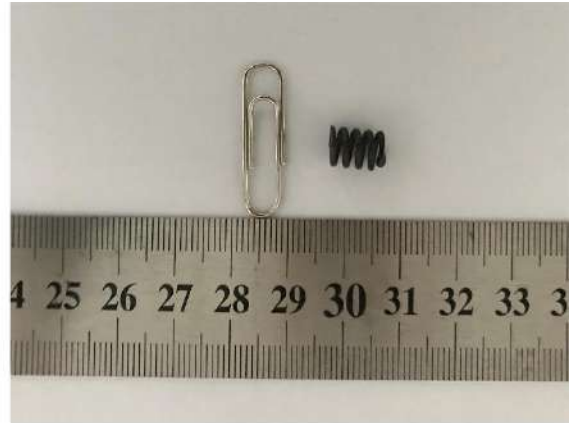
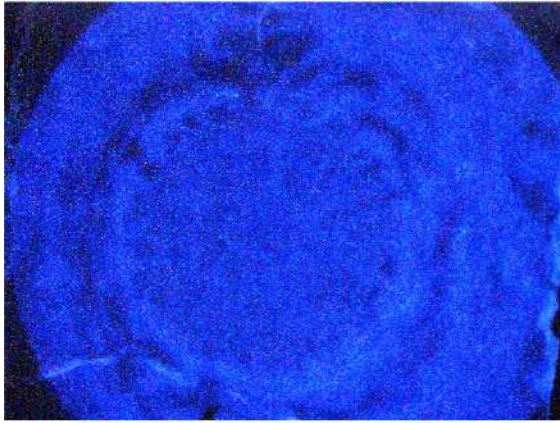


Supplementary Figure 14. Photon energy dependent attenuation coefficient of $(\text{PEA})_2\text{PbBr}_4$.

With the aid of XCOM web tool⁸, the photon energy-dependent linear attenuation coefficient of (PEA)₂PbBr₄ (dopant LiBr neglected) is plotted in Supplementary Figure 12. X-ray attenuation within an absorber follows the single exponential decay,

$$\frac{I}{I_0} = e^{-\mu t}$$

where I is the number of transmitted photon and I_0 is the photon number without absorber (the term $\frac{I}{I_0}$ can be considered as transmission), μ is the linear attenuation coefficient and t is the thickness of the absorber. The linear attenuation coefficient of (PEA)₂PbBr₄ at 8 keV (Cu K α , 1.54 Å) is 222 cm⁻¹ and the film thickness is 67 μm while single crystal 400 μm. Therefore, the respective transmission of film and single crystal are 22% and 0.014%. The single crystal is brighter under the same condition in our X-ray imaging and thus thicker film or crystal is needed.



Supplementary Figure 15. Luminescence of the 1:1 $\text{Li}-(\text{PEA})_2\text{PbBr}_4$ film and bright-field and X-ray images of a spring and a paper clip. The blue emission of the spin-coated film under X-ray was bright. The details of a paper clip and a spring inside an envelope can be seen in the X-ray images.

References

1. Shibuya, K., Koshimizu, M., Nishikido, F., Saito, H. & Kishimoto, S. Poly[bis(phenethylammonium) [dibromidoplumbate(ii)]-di- μ -bromido]]. *Acta Crystallogr., Sect. E: Crystallogr. Commun.* **65**, m1323-m1324 (2009).
2. Dorenbos, P. in *Radiation Detectors for Medical Applications*. (eds Stefaan Tavernier, Alexander Gektin, Boris Grinyov, & William W. Moses) 191-207 (Springer Netherlands).
3. Dorenbos, P., Haas, J. T. M. d. & Eijk, C. W. E. v. Non-proportionality in the scintillation response and the energy resolution obtainable with scintillation crystals. *IEEE Trans. Nucl. Sci.* **42**, 2190-2202 (1995).
4. Birowosuto, M. D. *Novel Gamma-Ray and Thermal-Neutron Scintillators: Search for High-Light-Yield and Fast-Response Materials*. (IOS Press, Amsterdam, 2008).
5. Eijk, C. W. E. v. *et al.* in *2008 IEEE Nuclear Science Symposium Conference Record*. 3525-3528.
6. Kawano, N. *et al.* Scintillating organic–inorganic layered perovskite-type compounds and the gamma-ray detection capabilities. *Sci. Rep.* **7**, 14754 (2017).
7. Birowosuto, M. D. *et al.* Li-based thermal neutron scintillator research; $\text{Rb}_2\text{LiYBr}_6: \text{Ce}^{3+}$ and other elpasolites. *IEEE Trans. Nucl. Sci.* **55**, 1152-1155 (2008).
8. NIST. *XCOM calculator*, <<https://www.physics.nist.gov/PhysRefData/Xcom/html/xcom1.html>> (2010).

Reprints and permissions information is available at www.nature.com/reprints